ABSTRACT

COFFER, BRICE EVAN. Impacts of Increasing Low-Level Shear on Supercells during the Early Evening Transition. (Under the direction of Matthew Parker).

The dynamical response to increasing low-level shear on mature simulated supercells is investigated using observed soundings during the early evening transition for three cases from the second Verification of the Origins of Rotation in Tornadoes Experiment (VORTEX2). Using a modeling technique called base-state substitution (BSS), supercells were simulated in both low and high shear environments. The primary effect of the increase in low-level shear is a non-linear response in the updraft strength due to the enhanced low pressure in the updraft from the spin of the mesocyclone. This is particularly important at low-levels, as the increased shear helps to establish the base of the mesocyclone at lower altitudes. This in turn increases the storm's ability to lift cool outflow air, which may have implications for tornadogenesis. Trajectories launched in developing vortices show that, when the low-level shear is increased, parcels experience greater vertical velocity and stretching due to increased dynamic accelerations, despite comparable buoyant accelerations.

Impacts of Increasing Low-Level Shear on Supercells during the Early Evening Transition

by
Brice Evan Coffer

A thesis submitted to the Graduate Faculty of
North Carolina State University
in partial fulfillment of the
requirements for the degree of
Master of Science

Atmospheric Sciences

Raleigh, North Carolina

2014

APPROVED BY:

_____   _____
Matthew Parker   Sandra Yuter
Committee Chair

_____
Gary Lackmann

BIOGRAPHY

Brice grew up in Houston, Texas. He graduated with honors from the University of Oklahoma in May 2012 with a Bachelor of Science in Meteorology. In addition to studying at OU, Brice also worked for the National Severe Storms Laboratory and interned at the Storm Prediction Center. He participated in several field programs, including VORTEX2. Brice's original interest in meteorology stemmed from tropical cyclones, however while working at NSSL and the SPC, as well as storm chasing throughout the Great Plains, he developed a deep passion for severe convective weather.

In his free time, Brice likes to watch TV and play video games. He also enjoys soccer, football, and kayaking.

ACKNOWLEDGMENTS

TABLE OF CONTENTS

LIST OF TABLES

LIST OF FIGURES

INTRODUCTION

Supercell mesocyclonic tornadogenesis has been described as a three-step process (Davies-Jones and Brooks 1993, Davies-Jones 2014). First, an updraft acquires rotation through tilting of environmental horizontal vorticity. Second, a downdraft produces vertical vorticity at the surface. Finally, a tornadic circulation spins-up at the ground as vortex lines in the storm's outflow are rearranged, converged, and stretched until they become vertically oriented throughout a significant depth (Walko 1993; Wicker and Wilhelmson 1995). This final step is still not easily anticipated, as several factors determine whether surface parcels with cyclonic vorticity will ascend to appreciable heights (Markowski et al. 2011, Markowski and Richardson 2014). Although most significant tornadoes are associated with supercells, most supercells do not produce tornadoes (Brooks et al. 1994; Trapp et al. 2005). Thus, one of the biggest remaining challenges in supercell research is discriminating between tornadic and non-tornadic supercells. Several environmental parameters have been shown to possess substantial skill in forecasting tornadogenesis. One such parameter that discriminates well between strongly tornadic supercells and non-tornadic supercells is the environmental shear vector magnitude[1] in the lowest kilometer above ground layer (AGL; Brooks et al. 2003; Markowski et al. 2003). Trying to understand the role of this low-level shear was a primary motivation for the present study.

Supercells exist in the presence large environmental wind shear, in which the mid-level mesocyclone forms through the process of tilting horizontally oriented vorticity into the vertical plane by the storm's updraft (e.g., Schlesinger 1975; Maddox 1976; Rotunno 1981,

---

[1] Hereafter referred to as bulk shear or simply shear.

Davies-Jones 1984). Considering this, it was once believed that low-level mesocyclones and tornadoes formed via a similar process. However, tilting in this 'in-up' manner cannot produce vorticity at low-levels because the ambient vortex lines only acquire an appreciable vertical component *as they are being advected upward* (Davies-Jones 1982; Davies-Jones and Markowski 2013). It has been shown through numerical and observational studies that solenoidally generated horizontal vorticity is the dominant contributor to low-level circulation in supercells (e.g. Rotunno and Klemp 1985; Davies-Jones and Brooks 1993; Alderman et al. 1999; Markowski et al. 2008; Markowski et al. 2012a,b). Parcels reaching the near-surface[2] vortex have a history of descent through the rear-flank outflow (Dahl et al. 2012). The crucial difference between the updraft and downdraft tilting processes is that parcels in a downdraft acquire vertical vorticity *as they are advected towards the surface*.

If the surface vorticity that develops into tornadoes is produced solely due to downdraft processes, then why are the kinematic properties of the inflow a statistically significant predictor of strong tornadoes? The respective roles of environmental and storm-generated vorticity have yet to be fully explained, although substantial progress has recently been made (Dahl et al. 2014, Markowski and Richardson 2014). A physical relationship or interaction that helps facilitate the transition between tornadogenesis step two and three has been hypothesized, likely due to dynamic effects from changes in the storm's profile of vertical vorticity. Wicker (1996) showed that the *orientation* of storm-relative environmental shear influences the development of strong low-level mesocyclones. However, the shear *magnitude* is most commonly used in operational forecasting parameters like the significant

---

[2] In this study, near-surface will refer to the lowest model levels (below 100 m), while low-level will refer to lowest 1-2 km AGL.

tornado parameter (STP; Thompson et al. 2003). Tornadic vortices appear to form when vorticity-rich outflow can be "processed" by the overlying updraft (Markowski and Richardson 2014). This is most likely to occur when the cold pool is less negatively buoyant and/or a strong vertical perturbation pressure gradient force exists (Markowski et al. 2002; Markowski and Richardson 2014). The amount of shear concentrated in the near-ground layer might be critically important for tornadic supercells because it governs the base height of the midlevel mesocyclone (Markowski et al. 2012b). A stronger mesocyclone at a lower altitude would allow the storm to forcibly lift and stretch negatively buoyant air from the rear-flank outflow through an upward-directed perturbation pressure-gradient force. In contrast, within three non-tornadic supercells, Markowski et al. (2011) found trajectories in the outflow that rose only a few hundred meters before abruptly decelerating. They hypothesized that in such case the perturbation pressure-gradient force was insufficiently strong (or even adverse), preventing parcels from being converged and stretched into a tornadic vortex.

The uncertain role of low-level environmental shear continues to motivate ongoing research. The second Verification of the Origins of Rotation in Tornadoes Experiments (VORTEX2; Wurman et al. 2012) collected unprecedented observations of numerous supercells. One mission of this campaign was to understand the spatial and temporal variability in the environment of supercells through numerous near-storm soundings (Parker 2014). When comparing the early-in-life versus late-in-life composite soundings, Parker (2014) found that, although the 0-6km shear vector magnitude remained nearly identical over time, the winds below 2-3 km AGL increased in speed near sunset. This resulted in dramatic

increases in low-level environmental bulk shear and storm-relative helicity (SRH). The tornado climatology in the United States shows that there is a maximum frequency of tornadoes during this time frame[3], especially in the Great Plains[4].

A commonly observed characteristic of severe weather events in the central United States is an increase in shear in the low-levels of the atmosphere during the late afternoon and early evening hours (Maddox 1993). The United States Great Plains exhibits a distinct maximum in the climatology of nocturnal low-level jets (LLJ; Bonner 1968; Song et al. 2005). Decoupling of the surface layer from the rest of the afternoon boundary layer during the early evening transition (EET) commonly causes a decrease in the surface wind speed (Nieuwsadt 1985) and the development of a LLJ (e.g. Blackadar 1957; Shapiro and Fedorovich 2010; van de Wiel et al. 2010). A defining characteristic of the LLJ is a veering of the wind vector with time and the development of a supergeostrophic wind maximum (Stull 1988). The associated changes in the magnitude and direction of the lower tropospheric wind shear are in turn potentially important to convective storm dynamics.

LLJs have been studied extensively due to their widespread impacts, including moisture transport linked to nocturnal rain maxima (Higgins et al. 1997), convection initiation (Trier and Parsons 1993), transport of pollutants (Banta et al. 1998), urban heat islands (Hu et al. 2013), and strong vertical wind shear. Research on the latter has mainly focused on aviation hazards (Proctor et al. 2000) and wind energy (Storm et al. 2008),

---

[3] Storm chasers often anecdotally refer to this phenomenon as "six-o'clock magic", because supercells seem to have the propensity to produce tornadoes in the early evening hours, as the sun sets. This may be associated with lower lifted condensation levels (LCL) in addition to the higher SRH (e.g. Parker 2014).
[4] These data are available from NCDC
(http://www.ncdc.noaa.gov/oa/climate/severeweather/tornadoes.html#timing)

however the early evening evolution of the boundary layer wind profile could have profound impacts on severe convective storms, as well as tornadoes (Fritsch et al. 1994; Maddox 1993). In fact, forecast discussions issued by the National Oceanic and Atmospheric Administration (NOAA) Storm Prediction Center (SPC) frequently mention a window of opportunity for increased probability of tornadogenesis during the EET due to LLJ-enlarged hodographs, before significant surface stabilization occurs and updrafts are no-longer surface based.

A complicating factor in understanding the EET with respect to supercells is that the EET has been predominately studied with cases that exhibit clear skies and light winds in order to distinctly isolate the signatures of the EET. The onset of the EET could be accelerated in the inflow sector of most supercells due to the storm blocking incoming solar radiation and thus triggering an earlier decoupling of the boundary layer (assuming the inflow sector exists to the east of the supercell). Numerical modeling studies that take into account the radiative cooling beneath the anvils of supercells reveal reductions in vertical mixing and stronger vertically sheared layers below 500 m, although this effect is less prevalent with faster storm motions (Frame and Markowski 2010, 2013). Soundings from near supercells (e.g. Parker 2014) also show strong wind speeds and shear in the boundary layer, which is rarely, if ever, documented in the EET climatology studies. It is unclear how storms directly respond to these changes in low-level shear during the EET, nor how changes in shear interplay with changes in stability.

The focus of this study is on the response of supercells' low-level updrafts to increasing low-level shear during the EET and the associated fate and amplification of near-

surface vertical vorticity. We hypothesize that the evolving low-level shear during the EET leads to changes in the low-level dynamic lifting of air in addition to changes in the storm's profile of vertical vorticity. This could have implications for tornadogenesis. To address this hypothesis, we employ idealized simulations based upon observed soundings from near VORTEX2 supercells that underwent EETs. Details regarding the methods are described in Section 2. Results and interpretation from the three VORTEX2 cases are offered in Section 3-5. A summary of the main conclusions and avenues for future work are presented in Section 6.

METHODS

a) Model Configuration

Limitations in cloud models and computational power have largely precluded in-depth analysis of the relationship between environmental shear and storm-generated vorticity until recently (Rasmussen 2003). As these limitations have been overcome, or at least minimized, the physical importance of observed forecast parameters can become more fully understood through high-resolution numerical simulations. The Bryan Cloud Model 1, commonly referred to as CM1 (Bryan and Fritsch 2002), is a sophisticated moist, non-hydrostatic model well suited to idealized cloud scale simulations. Using CM1 Release 17, storms were simulated in a 150 x 150 x 18 km^3, storm-relative domain with horizontal grid-spacing of 250 m for 5 hrs. The vertical grid-spacing was stretched from 50 m near the surface to 250 m aloft (lowest model level: 25 m). Fine vertical resolution near the surface is desirable in order to adequately resolve the supercells' low-level dynamics. The horizontally homogeneous simulations were initialized with observed soundings, based on three VORTEX2 cases that will be discussed further in subsection (c). Convection was initialized using the convergence mechanism described by Loftus et al. (2008). Time-splitting was employed for acoustic waves, with open, radiative boundary conditions employed on the small time steps for the lateral boundaries, following Klemp and Wihelmson (1978). Rigid, free slip boundary conditions were used on the lower and upper-boundaries, and a Rayleigh damping sponge layer was applied above 14 km. Radiation, surface fluxes and the Coriolis force were neglected for the simplicity of isolating key processes. In one recent study (Schenkman et al. 2014), frictionally generated vorticity was found to be a large contributor

to supercell tornadogenesis in a simulated case-study using data-assimilation. However, how best to apply surface drag in idealized simulations of sheared environments is not currently widely agreed upon and is the subject of future research. A simple treatment of precipitation microphysics, developed by Lin et al. (1983) and modified by the National Aeronautics and Space Administration (NASA) Goddard Cumulus Ensemble model (Tao and Simpson 1993), was chosen instead of more elaborate multi-moment schemes. Although any choice of parameterization will ultimately affect the four-dimensional structure of simulated convection, the general conclusions presented herein were insensitive to several microphysical parameterizations sensitivity tests, including the dual-moment Thompson (Thompson et al. 2008) and Morrison (Morrison et al. 2005) schemes, as well as the National Severe Storm Laboratory's variable graupel and hail density scheme (Mansell et al. 2010).

b) Base-State Substitution

The idealized, storm-scale modeling community has relied heavily on homogeneous base-state conditions in order to isolate and understand fundamental dynamical processes in convective storms (as reviewed comprehensively by Wilhelmson and Wicker 2002). Simulating convection in heterogeneous environments introduces several complicating factors, including the difficulty of assigning cause and effect to hypothesis tests. To address such concerns, Letkewicz et al. (2013) introduced a new modeling technique termed "base-state substitution" (BSS), which involves approximating temporal tendencies experienced by a storm by gradually changing the homogeneous base state. This allows the user to "investigate how a *mature* storm responds to a changing background environment, as opposed to how storms *develop* in different background environments" (Letkewicz et al.

2013). The BSS approach provides an ideal platform to test how a mature supercell responds to the EET. Once a supercell matured in the control simulation, the original base-state wind profile was gradually modified to have stronger low-level shear (as observed), evolving through intermediary observed soundings to the final observed profile. Comparisons will be made between the unmodified, control simulation and a higher shear BSS simulation.

Unless otherwise stated, in order to isolate the effect of increasing low-level shear on mature supercells, the BSS soundings were thermodynamically identical to the control sounding. The lower-level winds reflected the observed changes in low-level shear, while the upper-level winds in the BSS soundings are identical to the control sounding. The evolving low-level wind profile alone results in noticeable differences in common environmental forecast indices such as the supercell composite parameter and significant tornado parameter, despite identical thermodynamic fields and approximately equal deep layer shear, as shown in Table 2.1. The BSS process consisted of 10 soundings linearly interpolated from the original soundings, which were introduced over a span of 1 hr. This somewhat abridged BSS window provided a substantial period for comparisons before convection grew upscale in the control simulation. Sensitivity tests were performed varying the timing and duration of the base-state substitution process. Storm evolution was not radically dissimilar between the varying simulations, which is consistent with the findings reported by Letkewicz et al. (2013).

c) *VORTEX2 Case Studies*

Rarely have soundings been obtained *throughout* the life cycle of multiple supercells, especially into the evening transition. These observations allow us to test the hypothesis that

increases in low-level shear during the EET can result in a stronger low-level mesocyclone, and perhaps be beneficial for tornadogenesis. Since the supercell simulations in this study are idealized with horizontally homogeneous initial conditions that approximate the observed changes in the environmental wind profile, the goal of this research is *not* to reproduce the exact supercell or tornado observed during the cases described below, although some interesting comparisons exist (as reviewed in the results sections). As described below, subtle modification to the observed soundings were needed. Highly unstable environments (i.e. large lapse rates and strong shear) can exist in nature where continual surface heating and a large-scale pressure gradient reinforce the conditions, despite vigorous mixing. However, in an idealized model, there is no pressure-gradient force, surface heating, nor any friction to offset these energy sources. So, for example, here we slightly stabilize the temperature profile, which minimizes Kelvin-Helmholtz instability and preserves most of the low-level shear, without having to remove the total eddy mixing tendency in the model's equations, as has been attempted in previous studies[5].

i)   5 June 2009: "Goshen County" Tornadic Supercell

The Goshen County, Wyoming tornadic supercell of 5 June 2009 was selected as an ideal case, due to dense temporal and spatial sounding observations through the early evening hours. Three far inflow soundings were chosen to represent the base-state environment during the EET on 5-6 June 2009, at 2155, 2335, and 0057 UTC (Fig. 2.1). Only far inflow soundings were considered because Parker (2014) found enhancements in LCL height and

---

[5] Experiments, with and without the base-state eddy mixing tendency, were conducted, and they produced storms with evolutionary differences. Eliminating the mixing of the base-state environment is understandable in the far-field but could cause unknown, negative consequences in the storm.

SRH closer to supercells, presumably due to storm-generated feedbacks. The distance between each sounding was also considered because observed sounding changes following a supercell could be due to spatial environmental heterogeneity, instead of temporal evolution. For this case, the total distance between the launch points for the three soundings was 80 km. Heterogeneity of this magnitude is not currently resolvable for operational purposes (e.g. the 40 km grid-spacing of SPC mesoanalyses).

A few modifications to the control 2155 UTC sounding were necessary. Data collection from soundings in VORTEX2 was normally terminated approximately an hour after launch so that a new sounding could be released. During this hour, the balloons nearly reach the approximate height of the tropopause. For CM1 to run properly, stratospheric data needed to be approximated, thus a completely dry potential temperature inversion of 20 K/km with constant winds was chosen to represent this data gap. These choices above 10 km likely have little influence on the supercell, especially at low-levels. Potential temperature and mixing ratio were reset to be constant throughout the boundary layer based on their original mixed-layer values. The lowest levels were slightly stabilized by removing any super-adiabatic layers, helping to prevent spontaneous overturning at the smallest resolvable scales. Through trial and error, it was also determined that long-lived convection would only occur in the model when the dry, elevated mixed was slightly moistened from 2-4 km.

ii)   18 May 2010: "Dumas, Texas" Tornadic Supercell

Simulations were also performed using soundings collected during the Dumas, TX supercell from VORTEX2. Three far inflow soundings characterized the EET during 18-19 May 2010, 2257, 0044, and 0130 UTC (Fig. 2.2). The control 2257 sounding was modified

in a similar manner to the Goshen case, except no superadiabatic layers were present; therefore the boundary layer potential temperature was left unchanged. Due to the presence of a strong capping inversion, the layer at the base of the inversion was lifted 200 m up the sounding, such as might occur in response to synoptic lifting, as described in Markowski and Richardson (2010, see their Fig. 7.9). A larger domain (200 x 200 km^2) with lateral damping layers was required to ensure the simulated storm was not influenced by numerical noise. We speculate that the layer lifting, and thus the removal of the convective inhibition, contributed to more widespread perturbations compared to the Goshen case. The thermodynamics and upper-level winds were kept constant throughout the BSS process, however the winds below 4 km were altered to reflect the new wind profile at 0044 and 0130 UTC (compared to the Goshen case, 4 km provided a more natural breaking point than 6 km between similar values of both components of the wind in the three soundings).

iii)   *12 May 2010: "Clinton, Oklahoma" Tornadic Supercell*

A final case from VORTEX2 was selected for comparison. Two far inflow soundings were chosen to represent the Clinton tornadic supercell, 0039 and 0139 UTC on 13 May 2010 (12 May 2010 local time; Fig. 2.3). Modifications to the control 0039 UTC sounding in the boundary layer and stratosphere were similar to the Goshen and Dumas soundings described previously. An additional amount of stabilization was needed in order to suppress model instabilities due to the extreme amount of low-level shear observed on this day (Table 2.1c). The potential temperature was modified to increase by 2.5 K over the depth of the boundary layer (1.6 km), in order to keep the Richardson number near 0.25. A larger domain and lateral damping layers were also required, as in the Dumas case.

GOSHEN COUNTY SUPERCELL SIMULATIONS

The environment in southeast Wyoming on 5-6 June 2009 was characterized by a rather straight hodograph in the early afternoon, which gradually transitioned into a strongly curved hodograph in the early evening (Fig. 2.1). An upper-level ridge, situated over the central United States, began slowly propagating eastward, leading to strong, westerly flow over the northern High Plains. Throughout the day, several upper-level vorticity maxima traversed the region, providing large-scale lift (Fig. 3.1b). Slight backing of the surface winds in response to surface cyclogenesis in central Wyoming contributed to additional hodograph curvature during the EET. A tongue of warm, moist air at low-levels was being advected upslope into southeast Wyoming (Fig. 3.1a), further aiding the initiation of convection. Convective cells were initiated north of Cheyenne, Wyoming before 2000 UTC (Fig. 3.1c-f), and a well-documented tornadic supercell and EF2[6] tornado were well underway by 2200 UTC (e.g. Wakimoto et al. 2011, Atkins et al. 2012, Markowski et al. 2012a,b, Wakimoto et al. 2012, Wurman et al. 2012, Kosiba et al. 2013, Marquis et al. 2014). The supercell continued to move eastward in western Nebraska by 0000 UTC. The observed VORTEX2 soundings from 2155 UTC to 0057 UTC showed increases in the 1 km bulk shear, 0-1 km SRH, and 0-3 km SRH of approximately 6 m/s, 200 m^2/s^2, and 250 m^2/s^2, respectively (Table 2.1a).

a) Convection and Vorticity Evolution

To evaluate the effects of the EET on mature supercells, simulations using the observed soundings from VORTEX2 were performed, as described in Section 2. The lower

---

[6] Storm data available from the National Climatic Data Center storm events database (http://www.ncdc.noaa.gov/stormevents/)

shear Control simulation, using the 2155 UTC sounding, produces supercellular convection as was observed (Fig. 3.2), although due to the idealized modeling setup, comparisons to the observed supercell are necessarily superficial. Both the lower shear Control storm and the higher shear BSS storm maintain "classic" supercell structures through the first hour and a half after BSS (Fig. 3.2). Eventually, the outflow from the Control storm undercuts the updraft, leading to the demise of the control supercell and a more disorganized multicellular structure (not shown). The BSS storm remains an isolated, intense supercell throughout the simulation. The hook-echo, weak-echo regions, and rightward propagation, all common radar features associated with supercells, were more pronounced in the higher shear BSS supercell.

Time-height plots of maximum low-level vertical vorticity for both simulations are shown in Fig. 3.3. The vorticity throughout the lower-levels of the storm (the lowest 2-4 km) increased by approximately 50% after BSS. This indicates an overall strengthening of the low-level mesocyclone, as expected due to the enhanced storm-relative helicity. Both the lower shear Control and higher shear BSS supercells consistently produce appreciable near-surface vertical vorticity (greater than 0.04 s^{-1}). However, the higher shear BSS supercell produces a near-surface vortex that strengthens to almost 0.2 s^{-1} soon after the completion of the BSS process, which is twice as strong as any produced by the Control storm. These results are particularly interesting because, as mentioned earlier, the factors that control the amplification of surface vorticity are still unclear. The low-level wind profile is the only element that differs between the two model runs. Even though these simulations are not tornado-resolving, it appears that simply elongating the hodograph in the low-levels can play a major role in the development of strong surface vorticity.

b) Updraft Intensification

The higher shear BSS storm has a stronger maximum updraft throughout the lower and middle troposphere, by roughly 10 m/s (Fig. 3.4). The core of the updraft (vertical velocities greater than 20 m/s) descends to lower altitudes (Fig. 3.4), which presumably helps to establish the base of the mesocyclone closer to the surface (Fig. 3.3). Not only does the updraft strengthen at low-levels, it also acquires a greater areal extent over time (Fig. 3.5). Since environmental buoyancy was unchanged during BSS, these updraft differences must be due to either the dynamical effects of enhanced shear, or due to emerging differences in the simulated cold pools. In our simulations, the averaged potential temperature perturbation of the outflow was actually slightly smaller in the higher shear BSS run (Fig. 3.6), implying that updraft enhancement was not driven by enhanced cold pool lifting. Meanwhile, in the vicinity of the near-surface vortices, the outflow temperature was not noticeably different between the two simulations (Fig. 3.6). During the development of the most intense near-surface vortex in the higher shear BSS supercell (t ≈ 2.8 h), both the storm-averaged and near-vortex outflow were within 1 K of the lower shear Control simulation (not shown).

Because the cold pool hypothesis was not explanatory, we next assessed the lifting of air due to the dynamic component of the vertical pressure perturbation gradient acceleration (VPPGA). Employing the formulation described by Markowski and Richardson (2010), pressure perturbations (*p'*) for well-behaved fields on the storm-scale are given by (mean and perturbation quantities are denoted with an overbar and prime, respectively):

$$p' \propto e_{ij}'^2 - \frac{1}{2}\left|\boldsymbol{\omega}'\right|^2 + 2\overline{\boldsymbol{S}} \cdot \nabla_h w' - \frac{\partial B}{\partial z} \tag{1}$$

wherein the first two terms on the right hand side (rhs) are the nonlinear dynamic pressure perturbation terms and includes the deformation of the perturbation wind (deformation tensor: e'_{ij}) and the total vorticity of the perturbation wind ($\boldsymbol{\omega}'$). Deformation or divergence always yields positive pressure perturbations, commonly referred to as splat. Rotation (spin) is linked to low pressure. The third term on the rhs is the linear dynamic pressure perturbation term and is associated with an updraft (w) in environmental wind shear ($\boldsymbol{S}$). Low (high) pressure forms downshear (upshear) of the existing updraft. The final term on the rhs is the buoyancy (B) pressure perturbation term. The VPPGA can be calculated by solving iteratively for p' and then calculating the vertical derivative of p'.

Changes in the dynamic VPPGA were calculated for both the 0-1 and 0-3 km layers in a 20 x 20 km box following the supercell's mesocyclone. Pressure analysis was only performed while both simulations maintained supercell-like structures in the model output reflectivity field. In terms of both the box-averaged and box-maximum values, a much stronger dynamic VPPGA was observed at low-levels in the higher shear BSS storm compared to the lower shear Control storm (Fig. 3.7). The maximum values in both the 0-1 and 0-3 km layers increased by approximately 0.1 m/s^2 (i.e. an extra 10 m/s in less than two minutes). The areal extent of intense 0-1 km VPPGA values also greatly increases in size as the storm encounters higher environmental low-level shear (Fig. 3.8). The buoyant VPPGA remained steady throughout the BSS process and values were generally three times lower than dynamic VPPGA (Fig. 3.9). Given that CAPE was unchanged across the experiments; it is therefore not surprising that the dynamical effects of shear dominate the updraft differences.

16

One important effect of increased shear may be to establish the base of the low-level mesocyclone at lower altitudes. This idea was presented by Markowski et al. 2012b, who analyzed observed mobile radar data from the same "Goshen County" VORTEX2 case (5 June 2009), and supported by idealized toy-model simulations in Markowski and Richardson (2014). The vertical vorticity (ζ) equation, neglecting the Coriolis force, baroclinic effects, and friction is:

$$\frac{\partial \zeta}{\partial t} = -\boldsymbol{v} \cdot \nabla \zeta + \boldsymbol{\omega} \cdot \nabla w$$

(2)

where the first term on the rhs represents advection of vertical vorticity by the three-dimensional velocity vector (*v*), and the second term combines both the tilting and stretching of the vorticity vector by an updraft. When Eq. 2 is linearized, following Markowski and Richardson (2010), the relationship between the environmental shear and tilting is clearer conceptually:

$$\frac{\partial \zeta'}{\partial t} = -\bar{\boldsymbol{v}} \cdot \nabla_h \zeta' + \boldsymbol{k} \cdot (\boldsymbol{S} \times \nabla_h w')$$

(3)

where the first term on the rhs is the advection of the perturbation vertical vorticity by the mean horizontal velocity vector, and the second term is tilting of vorticity from the environmental wind shear by the gradient in updraft velocity. Assuming that updraft width is unchanged (so that $\nabla_h w'$ scales with w'), the tilting rate of horizontal vorticity into the vertical is proportional to the amount of environmental shear present multiplied by the updraft intensity. For a given updraft intensity, the more shear present, the faster horizontal vorticity will be tilted into the vertical. This, in turn, produces mesocyclonic values of

vertical vorticity (i.e. 0.01 s^{-1}) closer to the ground. This lowering of the base of the mesocyclone can be seen in both Figs. 3.3 and 2.4. Increasing values of vertical vorticity aloft can then feedback on the updraft velocity through non-linear dynamic pressure perturbations (i.e. the spin term in Eq. 1). Calculations reveal that the intensification of the dynamic forcing is dominated by these non-linear dynamic pressure perturbations (time-averaged 0-1 km maximum: 0.26 m/s^2), as opposed to the linear updraft-in-shear effect (time-averaged 0-1 km maximum: 0.05 m/s^2). There is also a compounding effect of this non-linear interaction. Since increased shear strengthens the updraft, this further enhances the tilting rate by the supercell's updraft, which can generate even stronger dynamic lifting. This is possibly why the storm averaged dynamic VPPGA in Figure 3.7 shows an increasing trend as time goes on.

Although the focus of this study is the low-level processes that are important to the tornadogenesis process, it is intriguing to briefly investigate the updraft intensification throughout the storm's depth (approximately 12 km). Parcel trajectories were launched in the inflow sector of both the lower and higher shear supercells, and velocity budgets were interpolated along the 20 trajectories that acquired the largest vertical velocity at 2 km. A larger positive dynamic contribution to the vertical velocity exists at low-levels in the higher shear supercell (Fig. 3.10). Throughout the rest of the troposphere, the dynamic contribution is near zero in the higher supercell, while is highly negative in the lower shear supercell (Fig. 3.10). In the upper-levels, the trajectories in the higher shear supercell traverse a different part of the storm further downstream than the lower shear (not shown). With a titled mesocyclone, there are larger values of dynamic acceleration downstream. This explains why

these 20 trajectories acquired less negative dynamic acceleration in the higher shear. To fully explain the behavior of the velocity field above 6 km, a more robust analysis would be required, possibly including many more trajectories and spatially averaging the trajectories (instead of simple time average). This is the subject of future work.

c) Trajectory Analysis

The final step in the tornadogenesis process involves rearranging, converging, and stretching vortex lines into a tornadic circulation. To evaluate the ingestion of vorticity-rich outflow by the supercell's overlying updraft, several million parcels were released in the cold pool of both the lower and higher shear Goshen simulations 15 minutes after the base-state substitution process was completed. Forward trajectories are done natively in CM1. The integration time step is equal to the model time step (2 s); output was saved every 10 s for 30 minutes. To ensure the analyzed trajectories were outflow parcels with appreciable vertical vorticity, they were filtered with the criteria of a -2.5 K temperature perturbation and 0.03 s^{-1} vertical vorticity at the bottom model level. Despite similar initial buoyancy, approximately 40% more outflow parcels acquired appreciable near-surface vorticity in the higher shear BSS supercell (1004 vs. 619). Comparing outflow parcels with *identical* initial buoyancy shows that outflow parcels in the higher shear BSS supercell generally rose to much greater heights and experienced greater vertical velocities and stretching of vorticity than their counterparts in the lower shear Control supercell (Fig. 3.11). This indicates a more favorable configuration for the final step of tornadogenesis in the higher shear BSS supercell.

An additional set of trajectories was launched when both simulations were producing a near-surface vortex. In order to determine the fate of the parcels that entered the developing

vortex, these parcels were densely launched in 3 x 3 x 1 km box surrounding the vortex and integrated forward until the vortex dissipated. Trajectories were filtered based on which vortex parcels acquired the most vertical vorticity at the bottom model level. Shown in Figures 3.12-3.14 are the twenty vortex parcels that acquired the most vertical vorticity at the bottom model level in each simulation. The vortex trajectories that acquired large near-surface vorticity often stagnated in the lower shear Control supercell and were advected towards the rear of the storm (Fig. 3.12), instead of rising vertically and participating in the overlying updraft, as in the higher shear BSS supercell (Fig. 3.13). The vortex trajectories in the lower shear Control supercell are indicative of a decoupling of surface cyclone from the parent updraft and mesocyclone, and thus a cessation or disruption of the vortex stretching (Trapp 1999). Similar trajectory behavior has been observed in nontornadic supercells (Markowski et al. 2011; see their Fig. 7).

Bulk statistics for the vortex trajectories shed light on why the near-surface vorticity in the higher shear BSS simulation strengthened to almost double that of the lower shear Control simulation. Despite similar outflow temperatures (within 1 K), parcels in the higher shear BSS storm rose faster and higher, increasing the stretching of vorticity (Fig. 3.14). The mean buoyant accelerations experienced by the parcels were similar in both simulations; however, the mean dynamic acceleration was almost three times as high in the higher shear BSS storm (Fig. 3.14). Thus, it stands to reason, that the near-surface vortex in the higher shear BSS supercell strengthened considerably more than the lower shear Control supercell due to the enhanced vertical stretching from a stronger VPPGA at low-levels, which was caused by the increasing low-level shear.

It is worth briefly mentioning the volatility of near-surface vorticity development in these simulations. The vortices that develop are small in scale and rarely last more than a few minutes. Additionally, seemingly minor changes in the initial conditions and model setup can cause deviations in the evolution of near-surface vorticity due to the highly nonlinear nature of vortex development. This volatility could be due to numerical procedures and settings, including the non-tornado resolving 250 m grid-spacing, the lack of surface drag, the zero-gradient bottom boundary condition, and/or the simplified microphysics. Arguably, the supercell simulations in the literature that produce the most realistic, long-lasting vortices employ data assimilation to highly constrain the development of convection (e.g. Xue et al. 2014). Recently a long lasting tornado-like vortex was also simulated using a similar idealized setup to this study, except with 30 m grid-spacing and double moment Morrison microphysics (Orf et al. 2014). It is possible that grid-spacing may be a major contributor to vortex duration. Since the vortices in this study only span a couple grid points, they are heavily diffused. Even interpolating the horizontal velocity components to the scalar grid points reduces the magnitude of the maximum near-surface vorticity by a factor of two. Additionally, the exclusion of surface drag prevents near-surface vortices from fully contracting into a tornado by disrupting cyclostrophic balance and inducing strong radial inflow (Davies-Jones 2014). Without friction in the current model setup, the pressure gradient is balanced by the centrifugal force and the near-ground inflow, paradoxically, never reaches its maximum intensity (Davies-Jones 2014).

d) Thermodynamic and Stabilization Experiments

In order to isolate the role of the low-level wind profile in the preceding simulations, no thermodynamic changes were implemented during the BSS process. However, the evolution of the wind field during the EET is intrinsically linked to changes in the temperature profile. Another higher shear BSS simulation was performed that reflected *both* the thermodynamic and kinematic transition observed in the VORTEX2 soundings, although the thermodynamic changes were rather small (Figs. 3.15, 3.16). Even under the observed stabilization, the supercell's mesocyclone responded very similarly by intensifying, lowering in altitude (Fig. 3.17), and expanding spatially due to increases in the non-linear component of the dynamic VPPGA (not shown).

Since the observed stability changes were quite small, a supplementary suite of simulations were performed using artificial stabilization described in Parker (2008) and improved upon in French and Parker (2010). The aim was to address the following question: How much stabilization can a mature supercell endure? Starting at the initial time of BSS (t = 1.5 hr), for both the lower shear Control and higher shear BSS supercells, isothermal layers were progressively created by cooling the surface temperature by 2, 4, and 8 K at a rate of 3 K/hr.

In both the lower and higher shear cases, the simulations maintained the visual appearance of supercellular features, including a hook-echo, weak-echo regions, and rightward propagation, regardless of the strength of the statically stable layer (not shown). The mesocyclone strength was reduced at low-levels in the lower shear Control supercell but not until a significant amount of cooling had taken place (4 K; Fig. 3.18). For the higher

shear BSS supercell, the positive influence of the increasing low-level shear on the mesocyclone offsets the negative influence of decreased surface buoyancy (Fig. 3.19). The most noticeable difference in the simulations is the development of near-surface rotation. In the lower shear Control supercell, the generation of appreciable near-surface vorticity ceases after cooling greater than 2 K (Fig. 3.18) likely due to decreased baroclinity in the low-levels of the supercell (not shown). These trends build upon the conclusions of Nowotarski et al. (2011), who found that, as low-level static stability increased, the combination of decreases in convergence and low-level baroclinic vorticity generation contributed to weaker near-surface vertical vorticity maxima, despite the presence of a robust mesocyclone. As shear is increased in the BSS supercell, near-surface rotation is reduced but not eliminated (Fig. 3.19). This presents an operational challenge because forecasters rely on radar data above the surface to infer near-surface rotation (e.g. Davis and Parker 2014). These results suggest that link could be tenuous, especially given offsetting trends in shear and stability during the EET.

e) Summary

Considering all this, we believe that the most robust results of the higher shear BSS simulations for the Goshen EET case presented herein are the more "classic" reflectivity structures, the enhancement of the low-level mesocyclone, and the subsequent increase in low-level dynamic lifting. Given our current understanding of tornadogenesis, these would all favor the development of intense near-surface vortices, even though the development of near-surface vorticity in this model setup is somewhat volatile. Future work will look into

improving the model setup, including finer grid-spacing, surface drag, and advanced microphysics.

DUMAS SUPERCELL SIMULATIONS

The evolution of the wind profile in the Texas Panhandle on 18-19 May 2010 was similar to the Goshen case, with a distinct increase in speed and veering of the winds below 2-3 km AGL during the early evening hours. The hodograph during the late afternoon was predominately straight above 300 m, and over time this evolved into a highly curved hodograph (Fig. 2.2). The observed wind profile transition appears to be rather abrupt in the extant soundings due to several data communication issues that plagued the balloon launches between the 2257 and 0044 UTC soundings. As for the synoptic environment on this day, a negatively-tilted, upper-level trough slowly approached the central United States (Fig. 4.1b). Stronger mid-to-upper level flow overspread the Texas and Oklahoma Panhandle region near peak heating with mixed layer CAPE values exceeding 2000 J/kg. The VORTEX2 armada targeted a developing supercell by 2200 UTC and continued sampling it as it moved east-northeastward (Fig. 4.1c-f). The supercell only managed to produce weak tornadoes from 2230-2330 UTC despite the visual presence of a strong, low-level mesocyclone (Skinner et al. 2014). As the supercell moved eastward, a stronger, EF2 tornado was documented at 0044 UTC (the same time as the first higher shear BSS sounding was observed; Fig. 2.2). The observed VORTEX2 soundings from 2257 to 0130 showed increases in the 1 km bulk shear, 0-1 km SRH, and 0-3 km SRH of approximately 6 m/s, 200 m^2/s^2, and 350 m^2/s^2, respectively (Table 2.1b). This case therefore complements the Goshen supercell study, having impressive low-level shear increases within an environment with slightly less CAPE and 0-6 km shear.

The lower shear Dumas Control simulation, using the 2257 UTC sounding, develops supercellular features within the first hour of the simulation and the mesocyclone frequently cycles throughout the next two hours, before ultimately dissipating (Fig. 4.2). At the time of BSS (t = 5400 s), the supercell is in the midst of cycling and no longer has an evident hook echo, despite large values of updraft helicity aloft. As the low-level shear increases in the BSS simulation, the hook echo is more persistent and the supercell stays more isolated. Pronounced transverse rolls caused by Kelvin-Helmholtz instability (due to very large low-level shear) rapidly contaminate the simulation for the higher shear BSS supercell after 3.5 hr (not shown). As such, the analysis for this case will be focused on the first 3.5 hr of the simulations.

The low-level mesocyclone response to the increase low-level shear is similar to the Goshen case (Fig. 4.3). Vertical vorticity values in the low-level mesocyclone increased by approximately 50%. The higher shear BSS supercell also readily produced intense near-surface vorticity. The strongest vortex in the higher shear BSS supercell strengthened to 0.25 s^{-1}, more than 2.5 times as strong as any near-surface vortex in the lower shear Control supercell. This again indicates that simply increasing the shear and storm-relative helicity during the EET can have profound impacts on the development of near-surface vorticity.

The higher shear BSS supercell also has a stronger, deeper, and wider updraft than the lower shear Control supercell (Figs. 4.4, 4.5). The lowering of the updraft, evident in Figure 4.4, occurs more rapidly than in the Goshen case likely because the first Dumas BSS sounding at 0044 UTC incorporates almost as much modification as the final Goshen wind profile (due to the time gap between observed soundings mentioned previously; Fig. 2.2). The storm-

averaged VPPGA shows immediate increases in the dynamic lifting due to the increased low-level shear. Within thirty minutes after the completion of the BSS process, the acceleration in the low-levels is several times stronger than the lower shear Control supercell (Fig. 4.6). The spatial extent of intense 0-1 km dynamic lifting is particularly increased in the vicinity of hook echo (Fig. 4.7). The contribution of the non-linear dynamic term to the low-level accelerations greatly exceeded the linear dynamic and buoyant terms (not shown). The increased lifting in the higher shear BSS supercell likely facilitated the development of a particularly intense near-surface vortex, where the vorticity intensified to 0.25 s^{-1} and vertical velocities greater than 25 m/s extended below 300 m (Figs. 4.3, 4.4). As in the Goshen case, outflow parcels with appreciable vorticity were more readily ingested into the parent updraft in the higher shear supercell compared to its lower shear counterpart (Fig. 4.8).

CLINTON SUPERCELL SIMULATIONS

The environment on 12-13 May 2010 was characterized by an upper-level, shortwave trough approaching the southern Great Plains, with a dryline situated in the eastern Texas Panhandle and a cold front surging south into northern Oklahoma. Supercellular convection was initiated ahead of the dryline in the Wichita Falls, Texas area but failed to maintain itself as it moved through southwest Oklahoma. Meanwhile, convection further west, near the triple point, quickly grew upscale. The VORTEX2 team targeted this line of convection with embedded supercells. After 0000 UTC, one particular supercell became dominant, and eventually produced an EF1 tornado near Clinton, Oklahoma during the EET at approximately 0130 UTC. Prima facie, the differences in the two wind profiles look minimal (Fig. 2.3). However, the observed VORTEX2 soundings from 0039 UTC to 0139 UTC showed increases in the 1 km bulk shear, 0-1 km SRH, and 0-3 km SRH of approximately 7 m/s, 150 m^2/s^2, and 100 m^2/s^2, respectively (Table 2.1c). One interesting aspect of the Clinton case is that the 0039 control sounding displays higher low-level shear than either of the final BSS soundings in the Goshen and Dumas cases. The low-level shear increases even further an hour later. As discussed in section 2c), the extreme amount of low-level shear present on this day complicates the idealized modeling approach used herein.

Simulations were attempted with several permutations of the observed soundings. The lower shear Control supercell achieved a steady state when the static stability in the boundary was increased so that the bulk Richardson number was approximately 0.25. However, the increase in low-level shear during the BSS process still led to Kelvin-Helmholtz instability, which disrupted the inflow into the supercell and ultimately lead to its

demise (Fig. 5.1). More extreme modifications to the base-state profile might have made the simulation viable but were considered undesirable. At some point, the excessive tuning overwhelms the benefits of using observed soundings.

Our preliminary assessment of the Clinton experiments was that, in environments that already possess very large vertical shear, further increases in low-level shear may actually be *disruptive* to a supercell. However, it is clear that a more sophisticated model setup (likely including parameterizations for surface drag and boundary layer turbulent mixing) is needed for such strongly sheared environments. This will be a topic of future research.

SYNTHESIS

In this article, we investigated the role of increasing low-level shear on mature supercells during the EET using observed soundings from VORTEX2. Using BSS to gradually change the base-state, supercells were simulated in both low and high shear environments for three different VORTEX2 cases (although only two produced usable results). Previous work has indicated a relationship between strong low-level shear and the development of intense near-surface vorticity in supercells. Our simulations using observed soundings show that:

1) As low-level shear increases, the supercell stays more organized and displays more coherent supercellular features, such as a hook-echo, weak-echo regions, and rightward propagation.

2) The vertical vorticity throughout the depth of the storm was greatly enhanced, indicating that both the low-level and mid-level mesocyclones were enhanced by the increasing low-level shear.

3) The supercells produced appreciable near-surface vertical vorticity in their *outflow*; however, the near-surface vortices were amplified as an indirect result of the shear in the *inflow* increasing during the BSS process.

4) The updraft was more intense at low-levels due to the increased dynamic VPPGA associated with larger vertical vorticity within the supercell's updraft.

5) Vorticity-rich outflow air was more readily ingested by the supercell's overlying updraft in the higher shear supercells, despite similar buoyancy. Increased

dynamic accelerations and vorticity stretching contributed to the surface vortices strengthening compared to the lower shear supercells.

6) When stabilization was introduced in order to emulate nocturnal cooling, the increases in low-level shear compensated for the decrease in buoyancy. The intensity of the low-level updraft and near-surface rotation was only diminished after significant cooling had occurred.

In light of these results, we revisit the question posed in section 1: since tornadoes are an outflow phenomenon, why are the kinematic properties of the inflow a statistically significant predictor of strong tornadoes? These results suggest the dynamical underpinning for the operational utility of low-level shear is an indirect facilitation between tornadogenesis steps two and three (described in section 1). *The primary response of increasing low-level shear is to strengthen, widen, and lower the base of the mesocyclone, inducing stronger dynamic lifting that could forcibly lift outflow with appreciable vorticity.* The trend of more intense near-surface rotation with increasing low-level shear fits with our current understanding of tornadogenesis (as described in Davies-Jones 2014 and Markowski and Richardson 2014). Positive vertical vorticity is transported towards the surface in "rivers" of cyclonic vorticity (Dahl et al. 2014) associated with surges of outflow (often referred to as secondary rear-flank gust fronts in observed storms; Marquis et al. 2008; Kosiba et al. 2013). The strong dynamic lifting provides a broad, persistent area where "tornadogenesis-ready" vorticity can easily be concentrated and then subsequently stretched while participating in the parent updraft. The dynamical effects of shear upon lifting of outflow parcels via this

pathway would not be sensitive to whether or not friction and complex microphysics are included.

Nevertheless, the detailed sensitivities of the tornadogenesis process cannot be fully elucidated from this study. In future work we plan to address the limitations imposed by the grid-spacing, lack of surface drag, and relatively simple microphysics parameterization. Storm-scale data assimilation could be used to constrain the development of convection so that the simulated supercells in these VORTEX2 case studies are more similar to their real-life counterparts. Finally, there are other temporally varying factors that may influence the tornadogenesis process besides low-level shear, including the lower tropospheric humidity, low-level CAPE, and the hodograph shape. The long range goal of this effort is to advance our understanding of how environmental conditions influence within-storm processes, including tornadogenesis.

REFERENCES CITED

Adlerman, E. J., K. K. Droegemeier, and R. P. Davies-Jones, 1999: A numerical simulation of cyclic mesocyclogenesis. *J. Atmos. Sci.*, **56**, 2045–2069.

Atkins, N. T., A. McGee, R. Ducharme, R. M. Wakimoto, and J. Wurman, 2012: The LaGrange Tornado during VORTEX2. Part II: Photogrammetric Analysis of the Tornado Combined with Dual-Doppler Radar Data. *Mon. Wea. Rev.*, **140**, 2939–2958.

Banta, R. M., and Coauthors, 1998: Daytime buildup and nighttime transport of urban ozone in the boundary layer during a stagnation episode, *J. Geophys. Res.*, **103**, 22519–22544,

Blackadar, A. K., 1957: Boundary layer wind maxima and their significance for the growth of nocturnal inversions, *Bull. Amer. Meteor. Soc.*, **38**, 282-290.

Bonner, W. D., 1968: Climatology of the Low Level Jet. *Mon. Wea. Rev.*, **96**, 833–850.

Brooks, H. E., J. W. Lee, and J. P. Craven, 2003: The spatial distribution of severe thunderstorm and tornado environments from global reanalysis data. *Atmos. Res.*, **67-68**, 73-94.

Bryan, G. H., and J. M. Fritsch, 2002: A benchmark simulation for moist nonhydrostatic numerical models. *Mon. Wea. Rev.*, **130**, 2917–2928.

Bunkers, M. J., Brian A. K., J. W. Zeitler, Richard L. Thompson, and Morris L. Weisman, 2000: Predicting Supercell Motion Using a New Hodograph Technique. *Wea. Forecasting*, **15**, 61–79.

Dahl, J. M. L., M. D. Parker, and L. J. Wicker, 2012: Uncertainties in Trajectory Calculations within Near-Surface Mesocyclones of Simulated Supercells. *Mon. Wea. Rev.*, **140**, 2959–2966.

Dahl, J. M. L., M. D. Parker, and L. J. Wicker, 2014: Imported and Storm-Generated Near-Ground Vertical Vorticity in a Simulated Supercell. *J. Atmos. Sci.*, **71**, 3027–3051.

Davies-Jones, R. P., 1982: Observational and theoretical aspects of tornadogenesis. *Intense Atmospheric Vortices*, L. Bengtsson and J. Lighthill, Eds. Springer-Verlag, 175–189.

Davies-Jones, R. P., 1984: Streamwise Vorticity: The Origin of Updraft Rotation in Supercell Storms. *J. Atmos. Sci.*, **41**, 2991–3006.

Davies-Jones, R. P., and H.E. Brooks, 1993: Mesocyclogenesis from a theoretical perspective. *The Tornado: Its Structure, Dynamics, Prediction, and Hazards, Geophys. Monogr.*, No. 79, Amer. Geophys. Union, 105–114.

Davies-Jones, R. P., and P. Markowski, 2013: Lifting of Ambient Air by Density Currents in Sheared Environments. *J. Atmos. Sci.*, **70**, 1204–1215.

Davies-Jones, R. P, 2014: A review of supercell and tornado dynamics, *Atmos. Res*. (2014), **In Press**. http://dx.doi.org/10.1016/j.atmosres.2014.04.007

Davis, J. M., and M. D. Parker, 2014: Radar Climatology of Tornadic and Nontornadic Vortices in High-Shear, Low-CAPE Environments in the Mid-Atlantic and Southeastern United States. *Wea. Forecasting*, **29**, 828–853.

Frame, J., and P. M. Markowski, 2010: Numerical Simulations of Radiative Cooling beneath the Anvils of Supercell Thunderstorms. *Mon. Wea. Rev.*,**138**, 3024–3047.

Frame, J., and P. M. Markowski, 2013: Dynamical Influences of Anvil Shading on Simulated Supercell Thunderstorms. *Mon. Wea. Rev.*, **141**, 2802–2820.

French, A. J. and M. D. Parker, 2010: The Response of Simulated Nocturnal Convective Systems to a Developing Low-Level Jet. *J. Atmos. Sci.*, **67**, 3384–3408.

Fritsch, J. M., J. D. Murphy, and J. S. Kain, 1994: Warm Core Vortex Amplification over Land. *J. Atmos. Sci.*, **51**, 1780–1807.

Higgins, R. W., Y. Yao, E. S. Yarosh, J. E. Janowiak, and K. C. Mo, 1997: Influence of the Great Plains Low-Level Jet on Summertime Precipitation and Moisture Transport over the Central United States. *J. Climate*, **10**, 481–507.

Hu, X., P. M. Klein, M. Xue, J. K. Lundquist, F. Zhang, and Y. Qi, 2013: Impact of Low-Level Jets on the Nocturnal Urban Heat Island Intensity in Oklahoma City. *J. Appl. Meteor. Climatol.*, **52**, 1779–1802.

Kain, J. S., and Coauthors, 2008: Some practical considerations regarding horizontal resolution in the first generation of operational convection-allowing NWP. *Wea. Forecasting*, **23**, 931–952.

Klemp, J. B., and R. B. Wilhelmson, 1978: The simulation of three-dimensional convective storm dynamics. *J. Atmos. Sci.,* **35,** 1070–1096.

Kosiba, K., J. Wurman, Y. Richardson, P. Markowski, P. Robinson, and J. Marquis, 2013: Genesis of the Goshen County, Wyoming, Tornado on 5 June 2009 during VORTEX2. *Mon. Wea. Rev.*, **141**, 1157–1181.

Lapworth, A., 2003: Factors determining the decrease in surface wind speed following the evening transition. *Q. J. R. Meteor. Soc.*, **129**, pp. 1945-1968.

Letkewicz, C. E., A. J. French, and M. D. Parker, 2013: Base-State Substitution: An Idealized Modeling Technique for Approximating Environmental Variability. *Mon. Wea. Rev.*, **141**, 3062–3086.

Lin, Y.-L., R. D. Farley, and H. D. Orville, 1983: Bulk parameterization of the snow field in a cloud model. *J. Climate Appl. Meteor.,* **22,** 1065–1089.

Loftus, A. M., D. B. Weber, and C. A. Doswell, 2008: Parameterized Mesoscale Forcing Mechanisms for Initiating Numerically Simulated Isolated Multicellular Convection. *Mon. Wea. Rev.*, **136**, 2408–2421.

Maddox, R. A., 1976: An Evaluation of Tornado Proximity Wind and Stability Data. *Mon. Wea. Rev.*, **104**, 133–142.

Maddox, R. A., 1993: Diurnal Low-Level Wind Oscillation and Storm-Relative Helicity. *The Tornado: Its Structure, Dynamics, Prediction, and Hazards, Geophys. Monogr*., No. 79, Amer. Geophys. Union, 591–598.

Mansell, E. R., C. L. Ziegler, E. C. Bruning, 2010: Simulated Electrification of a Small Thunderstorm with Two-Moment Bulk Microphysics. *J. Atmos. Sci.*, **67**, 171–194.

Markowski, P. M., J. M. Straka, E. N. Rasmussen, and D. C. Dowell, 1998a: Observations of Low-Level Baroclinity Generated by Anvil Shadows. *Mon. Wea. Rev*. **126**, 2942-2958.

Markowski, P. M., J. M. Straka, E. N. Rasmussen, and D. O. Blanchard, 1998b: Variability of storm-relative helicity during VORTEX. *Mon. Wea. Rev.,* **126**, 2959–2971.

Markowski P. M., J.M. Straka, and E. N. Rasmussen 2002: Direct surface thermodynamic observations within the rear-flank downdrafts of nontornadic and tornadic supercells. *Mon. Wea. Rev.*, **130**, 1692-1721.

Markowski, P.M., C. Hannon, J. Frame, E. Lancaster, A. Pietrycha, R. Edwards and R.L. Thompson, 2003: Characteristics of vertical wind profiles near supercells obtained from the Rapid Update Cycle. *Wea. Forecasting*, **18**, 1262-1272.

Markowski, P. M., J. M. Straka, E. N. Rasmussen, R. P. Davies-Jones, Y. Richardson, and J. Trapp, 2008: Vortex lines within low-level mesocyclones obtained from pseudo-dual-Doppler radar observations. *Mon. Wea. Rev.*, **136**, 3513–3535.

Markowski, P. M., and Y. P. Richardson, 2010: *Mesoscale Meteorology in Midlatitudes*, Wiley-Blackwell, 407.

Markowski, P. M., M. Majcen, Y. P. Richardson, J. Marquis, and J. Wurman, 2011: Characteristics of the wind field in three nontornadic low-level mesocyclones observed by the Doppler On Wheels radars. *E. Journal of Severe Storms Meteor,* **6**(3), 1–48.

Markowski, P., and Coauthors, 2012a: The Pretornadic Phase of the Goshen County, Wyoming, Supercell of 5 June 2009 Intercepted by VORTEX2. Part I: Evolution of kinematic and surface thermodynamic fields. *Mon. Wea. Rev.*, **140**, 2887–2915.

Markowski, P., and Coauthors, 2012b: The Pretornadic Phase of the Goshen County, Wyoming, Supercell of 5 June 2009 Intercepted by VORTEX2. Part II: Intensification of Low-Level Rotation. *Mon. Wea. Rev.*, **140**, 2916–2938.

Markowski, P. M., and Y. P. Richardson, 2014: The Influence of Environmental Low-Level Shear and Cold Pools on Tornadogenesis: Insights from Idealized Simulations. *J. Atmos. Sci.*, **71**, 243–275.

Marquis, J., Y. Richardson, J. Wurman, and P. Markowski, 2008: Single- and Dual-Doppler Analysis of a Tornadic Vortex and Surrounding Storm-Scale Flow in the Crowell, Texas, Supercell of 30 April 2000. *Mon. Wea. Rev.*, **136**, 5017–5043.

Marquis, J., Y. P. Richardson, P. M. Markowski, D. Dowell, J. Wurman, K. Kosiba, P. Robinson, and G. Romine, 2014: An investigation of the Goshen County, Wyoming,

tornadic supercell of 5 June 2009 using EnKF assimilation of mobile mesonet and radar observations collected during VORTEX2. Part I: Experiment design and verification of the EnKF analyses. *Mon. Wea. Rev.,* **142**. 530-554.

Morrison, H., J. A. Curry, and V. I. Khvorostyanov, 2005: A New Double-Moment Microphysics Parameterization for Application in Cloud and Climate Models. Part I: Description. *J. Atmos. Sci.*, **62**, 1665–1677.

Nieuwstadt, F. T. M. 1985: A model for the stationary, stable boundary layer. *Turbulence and diffusion in stable environments, J. C. R. Hunt, Ed., Oxford University Press*, 149-179.

Nowotarski, C. J., P. M. Markowski, and Y. P. Richardson, 2011: The Characteristics of Numerically Simulated Supercell Storms Situated over Statically Stable Boundary Layers. *Mon. Wea. Review*, **139**, 3139-3162.

Orf, L., R. Wilhelmson, and L. Wicker, 2014: Numerical Simulation of a Supercell with an Embedded Long-Track EF5 tornado. *Special Symposium on Severe Local Storms: The Current State of the Science and Understanding Impacts*, Atlanta, GA. [Available online at https://ams.confex.com/ams/94Annual/webprogram/Paper242579.html]

Parker, M. D., 2008: Response of Simulated Squall Lines to Low-Level Cooling. *J. Atmos. Sci.*, **65**, 1323–1341.

Parker, M. D., 2014: Composite VORTEX2 Supercell Environments from Near-Storm Soundings. *Mon. Wea. Rev.*, **142**, 508–529.

Parker, M. D., and J. M. Dahl, 2014: Production of near-surface vertical vorticity by downdrafts. *Mon. Wea. Rev.* **Submitted**

Proctor, F. H., D. A. Hinton, and R. L. Bowles, 2000: A windshear hazard index. Preprints, *Ninth Conf. on Aviation, Range, and Aerospace Meteorology*, Orlando, FL, Amer. Meteor. Soc., 7.7, pages 482-487. [Available online at http://ams.confex.com/ams/htsearch.cgi.]

Rasmussen, E. N., 2003: Refined Supercell and Tornado Forecast Parameters. *Wea. Forecasting*, **18**, 530-535.

Rotunno, R., 1981: On the evolution of thunderstorm rotation. *Mon. Wea. Rev.,* **109,** 577–586.

Rotunno, R., and J. B. Klemp, 1985: On the rotation and propagation of simulated supercell thunderstorms. *J. Atmos. Sci.*, **42**, 271–292.

Schenkman, A. D., M. Xue, and M. Hu, 2014: Tornadogenesis in a High-Resolution Simulation of the 8 May 2003 Oklahoma City Supercell. *J. Atmos. Sci.*, **71**, 130–154.

Schlesinger, R. E., 1975: A three-dimensional numerical model of an isolated deep convective cloud: Preliminary results. *J. Atmos. Sci.,* **32,** 934–964.

Shapiro, A., and E. Fedorovich, 2010: Analytical description of a nocturnal low-level jet. *Q. J. R. Meteorol. Soc.*, **136**, 1255-1262.

Skinner, P., C. Weiss, M. French, H. Bluestein, P. Markowski, and Y. Richardson, 2014: VORTEX2 observations of a low-level mesocyclone with multiple internal real-flank downdraft momentum surges in the 18 May 2010 Dumas, Texas supercell. *Mon. Wea. Rev.*, **142**, 2935-2960.

Song, J., K. Liao, R. L. Coulter, and B. M. Lesht, 2005: Climatology of the low-level jet at the southern Great Plains Atmospheric Boundary Layer Experiment Site. *J. Appl. Meteor.*, **44**, 1593-1606.

Storm, B., J. Dudhia, S. Basu, A. Swift, and I. Giammanco, 2009: Evaluation of the Weather Research and Forecasting model on forecasting low-level jets: Implication for wind energy. *Wind Energy*, **12,** 81–90.

Stull, R. B., 1988: *An Introduction to Boundary Layer Meteorology*. Kluwer Academic, 666 pp.

Tao, W.-K., and J. Simpson, 1993: The Goddard Cumulus Ensemble Model. Part I: Model Description. *Terrestrial, Atmospheric and Oceanic Sciences,* **4**, 19-54.

Thompson, G., P. R. Field, R. M. Rasmussen, and W. D. Hall, 2008: Explicit Forecasts of Winter Precipitation Using an Improved Bulk Microphysics Scheme. Part II: Implementation of a New Snow Parameterization. *Mon. Wea. Rev.*, **136**, 5095–5115.

Thompson, R. L., R. Edwards, J. A. Hart, K. L. Elmore, and P. Markowski, 2003: Close Proximity Soundings within Supercell Environments Obtained from the Rapid Update Cycle. *Wea. Forecasting*, **18**, 1243–1261.

Thompson, R. L., C. M. Mead, and R. Edwards, 2007: Effective Storm-Relative Helicity and Bulk Shear in Supercell Thunderstorm Environments. *Wea. Forecasting*, **22**, 102–115.

Trapp, R. J., 1999: Observations of nontornadic low-level mesocyclones and attendant tornadogenesis failure during VORTEX. *Mon. Wea. Rev.,* **127,** 1693–1705.

Trapp, R. J., G. J. Stumpf, and K. L. Manross, 2005: A Reassessment of the Precentage of Tornadic Mesocyclones. *Wea. Forecasting*, **20**, 680-687.

Trier, S. B., and D. B. Parsons, 1993: Evolution of Environmental Conditions Preceding the Development of a Nocturnal Mesoscale Convective Complex. *Mon. Wea. Rev.*, **121**, 1078–1098.

Van de Wiel, B. J. H., A. F. Moene, G. J. Steeneveld, P. Baas, F. C. Bosveld, and A. M. Holtslag, 2010: A Conceptual View on Inertial Oscillations and Nocturnal Low-Level Jets. *J. Atmos. Sci.*, **67**, 2679–2689.

Wakimoto, R. M., N. T. Atkins, and J. Wurman, 2011: The LaGrange Tornado during VORTEX2. Part I: Photogrammetric Analysis of the Tornado Combined with Single-Doppler Radar Data. *Mon. Wea. Rev.*, **139**, 2233–2258.

Wakimoto, R. M., P. Stauffer, W. Lee, N. T. Atkins, and J. Wurman, 2012: Finescale Structure of the LaGrange, Wyoming, Tornado during VORTEX2: GBVTD and Photogrammetric Analyses. *Mon. Wea. Rev.*, **140**, 3397–3418.

Walko, R. L., 1993: Tornado spin-up beneath a convective cell: Required basic structure of the near-field boundary layer winds. *The Tornado: Its Structure, Dynamics, Prediction, and Hazards, Geophys. Monogr.,* No. 79, Amer. Geophys. Union, 89–95.

Weisman, M. L., and J. B. Klemp, 1982: The dependence of numerically simulated convective storms on vertical wind shear and buoyancy. *Mon. Wea. Rev.*, **110**, 504–520.

Wicker, L. J., and R. B. Wilhelmson, 1995: Simulation and analysis of tornado development and decay within a three-dimensional supercell thunderstorm. *J. Atmos. Sci.,* **52,** 2675–2703.

Wicker, L. J., 1996: The role of near surface wind shear on low-level mesocyclone generation and tornadoes. Preprints, *18th Conf. on Severe Local Storms*, San Francisco, CA, Amer. Meteor. Soc., 115–119.

Wilhelmson, R. B, and L. J. Wicker, 2002: Numerical modeling of severe storms. *Meteor. Monogr.* C. A. Doswell III, Ed., American Meteorological Society, 123-166.

Wurman, J., D. Dowell, Y. Richardson, P. Markowski, E. Rasmussen, D. Burgess, L. Wicker, and H. B. Bluestein, 2012: The Second Verification of the Origins of Rotation in Tornadoes Experiment: VORTEX2. *Bull. Amer. Meteor. Soc.*, **93**, 1147–1170.

Xue, M., M. Hu, and A. D. Schenkman, 2014: Numerical Prediction of the 8 May 2003 Oklahoma City Tornadic Supercell and Embedded Tornado Using ARPS with the Assimilation of WSR-88D Data. *Wea. Forecasting*, **29**, 39–62.

TABLES AND FIGURES

Table 2.1: Summary of common environmental forecasting parameters calculated from the observed VORTEX2 soundings for a) 5 June 2009 "Goshen County" Tornadic Supercell, b) 18 May 2010 "Dumas, Texas" Tornadic Supercell, and c) 12 May 2010 "Clinton, Oklahoma" Tornadic Supercell. Environmental bulk layer shear vector magnitudes are simply referred to as "shear" (m/s). Storm-relative helicity (SRH; m2/s2) was calculated using the Bunkers storm motion (Bunkers et al. 2000). Both the convective available potential energy (CAPE; J/kg) and lifted condensation level (LCL; m) use the surface based parcel, and the supercell composite parameter and significant tornado parameter (dimensionless) utilize the effective inflow layer described by Thompson et al. 2007.

a) Goshen	6 km Shear	1 km Shear	1 km SRH	3 km SRH	CAPE	LCL	SCP	STP
CONTROL - 2155 UTC	30	6	84	142	2600	1130	8	2
BSS1 - 2335 UTC	31	7	115	219	2600	1130	13	4
BSS2 - 0057 UTC	30	12	279	381	2600	1130	29	8
b) Dumas	6 km Shear	1 km Shear	1 km SRH	3 km SRH	CAPE	LCL	SCP	STP
CONTROL - 2256 UTC	21	7	90	159	2132	880	8	2
BSS1 - 0044 UTC	23	12	284	429	2132	880	24	7
BSS2 - 0130 UTC	23	13	298	493	2132	880	27	8
c) Clinton	6 km Shear	1 km Shear	1 km SRH	3 km SRH	CAPE	LCL	SCP	STP
CONTROL - 0039 UTC	39	15	309	379	2376	1560	44	11
BSS - 0139 UTC	40	22	444	494	2376	1560	59	15
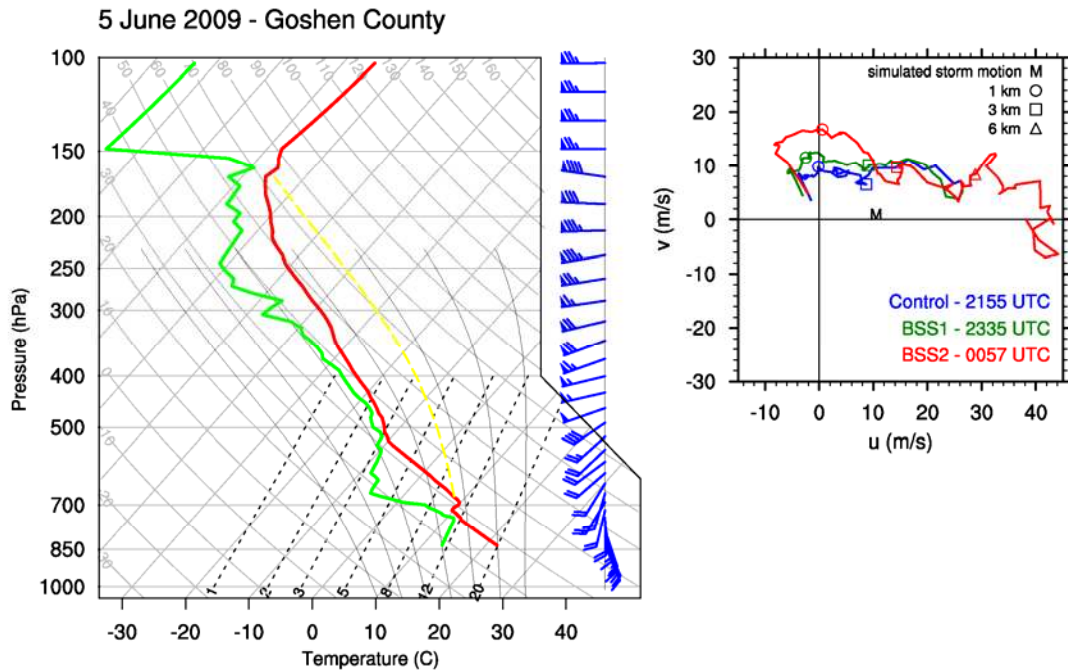
Figure 2.1: (left) Skew T-logp diagram and (right) hodograph showing the thermodynamic and kinematic environment used in the horizontally homogenous base-state substitution (BSS) simulations for the 5 June 2009 "Goshen County" Tornadic Supercell case. The Skew T-logp shows the 2155 UTC Control thermodynamics. The sounding displayed is directly from the model's initial conditions and the modifications to the Control sounding are described section 2c. Temperature is in red and dewpoint temperature is in green, while the dashed yellow line indicates the path of a surface based parcel above the level of free convection. The wind barbs on the Skew T-logp correspond to the Control sounding and are displayed in knots. On the hodographs, the 1, 3, and 6 km data points are denoted with symbols as shown, with the simulated storm motion plotted with "M". Control (blue), BSS1 (green), and BSS2 (red) wind profiles refer to the 2155, 2335, and 0057 UTC soundings respectively.
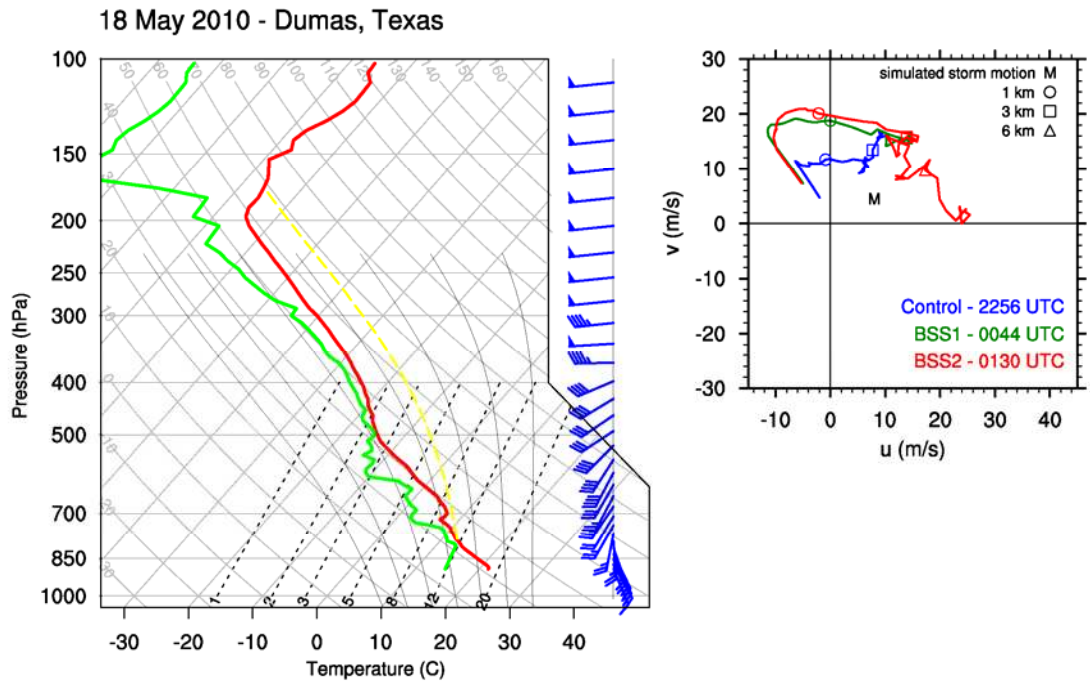
Figure 2.2: As in Figure 2.1, except for the 18 May 2010 "Dumas, Texas" Tornadic Supercell. Control, BSS1, and BSS2 wind profiles refer to the 2257, 0044, and 0130 UTC soundings respectively.
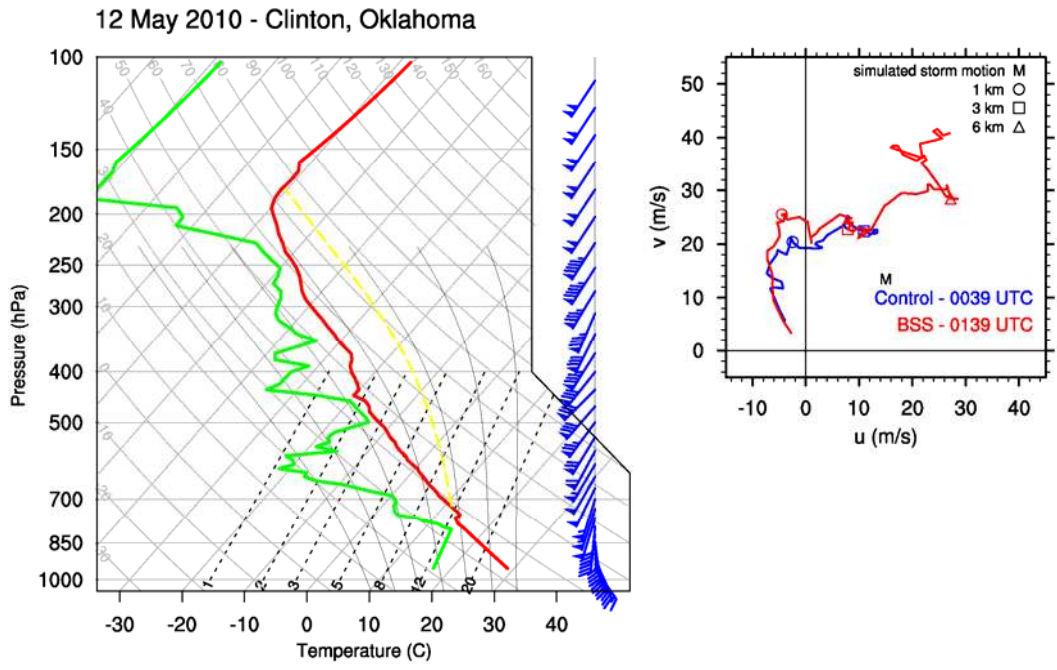
Figure 2.3: As in Figure 2.1, except for the 12 May 2010 "Clinton, Oklahoma" Tornadic Supercell. Control and BSS wind profiles refer to the 0039 and 0139 UTC (13 May 2010) soundings respectively.
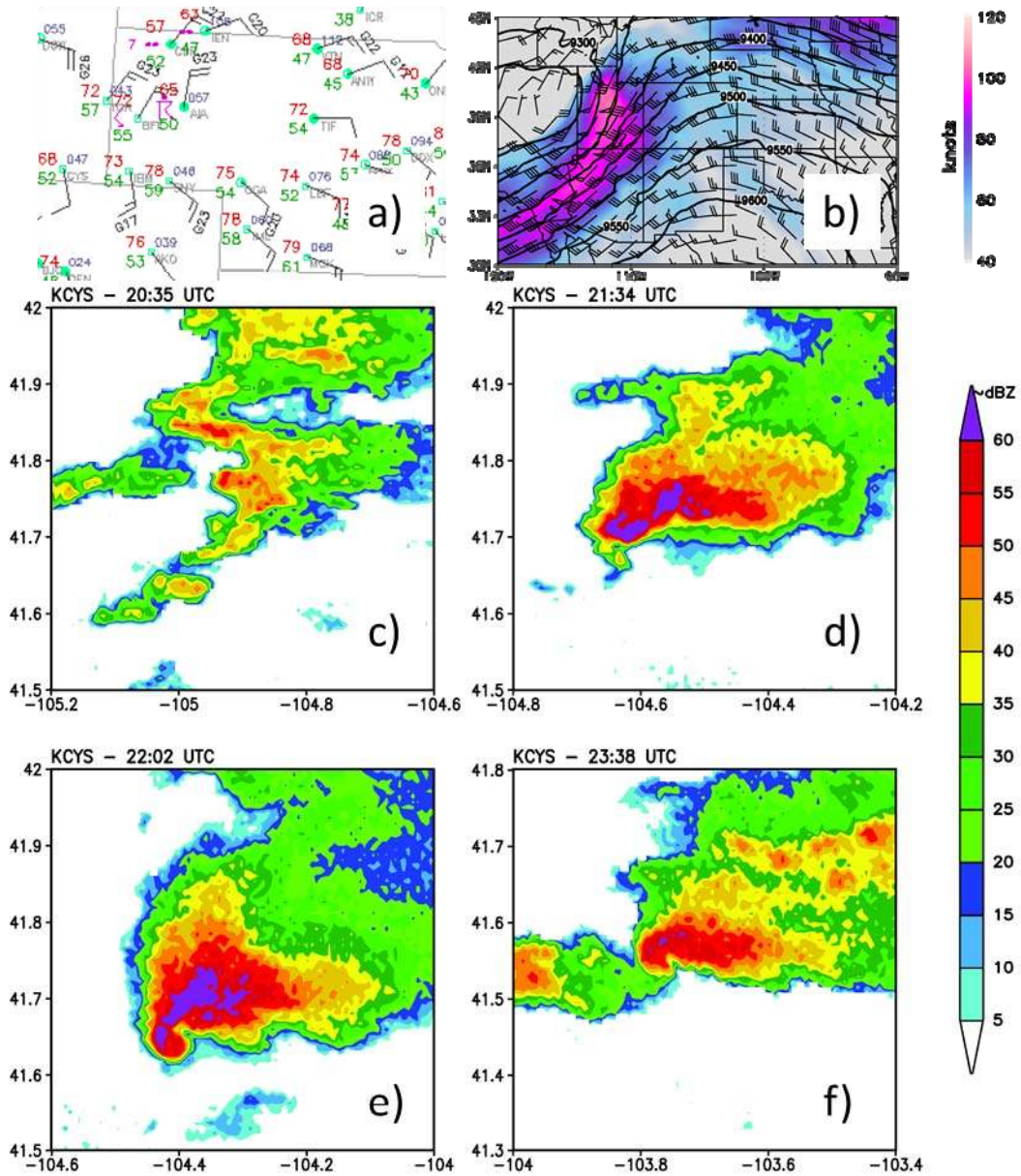
Figure 3.1: Synoptic overview for the 5 June 2009 "Goshen County" case. Panel a) shows the surface observations in the central United States at 0000 UTC on 6 June 2009. b) shows the 300 mb geopotential height field in m (contour) and wind speeds in knots (shaded, barbs). c) − f) show the observed base reflectivity from the KCYS WSR88-D.
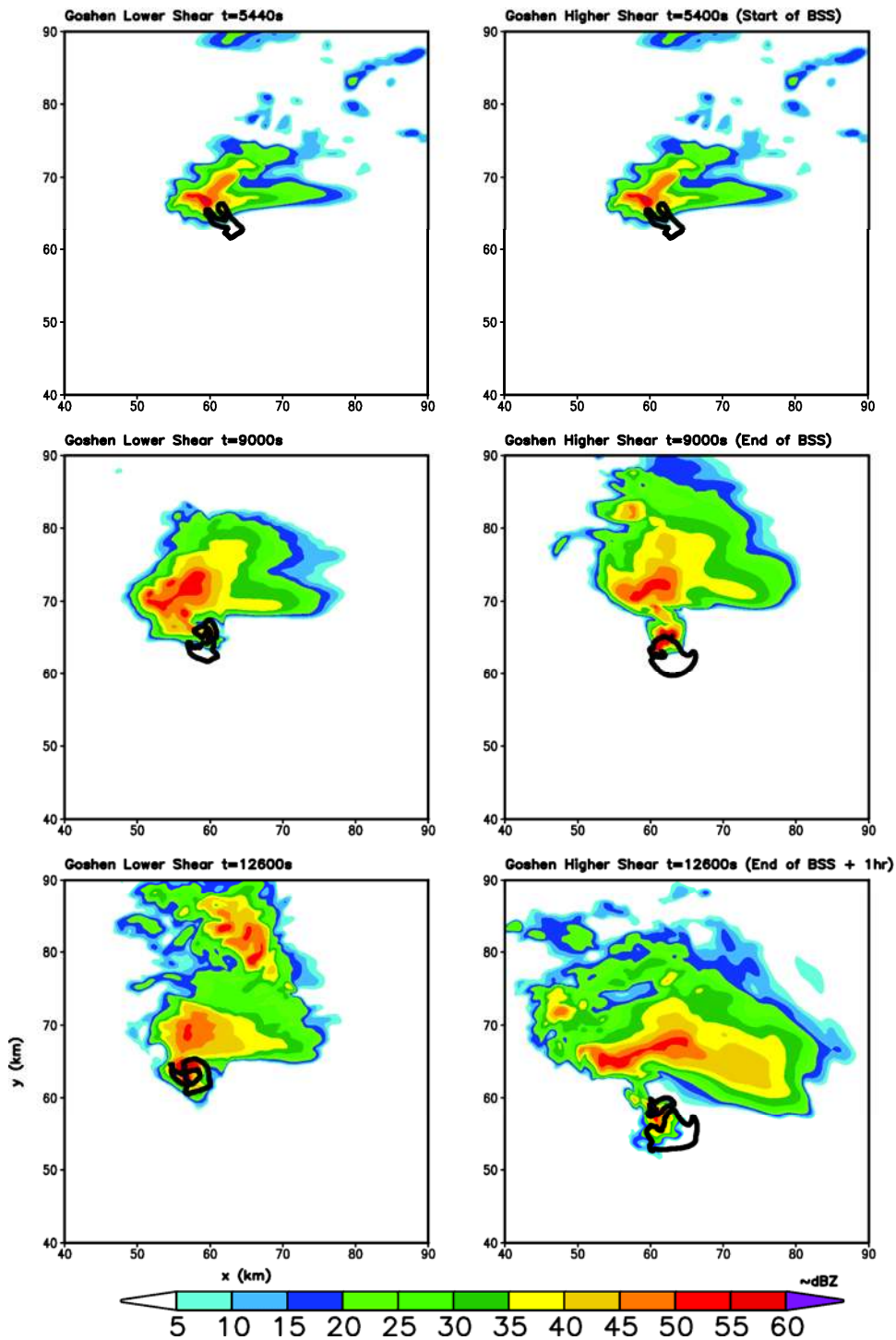
Figure 3.2: Model simulated base reflectivity for the lower shear Goshen Control simulation (left) and the higher shear Goshen BSS simulation (right) at the start of BSS, the end of BSS, and 1 h after BSS. The 500 m^2/s^2 1-6 km updraft helicity (defined by Kain et al. 2008) contour is shown in black.
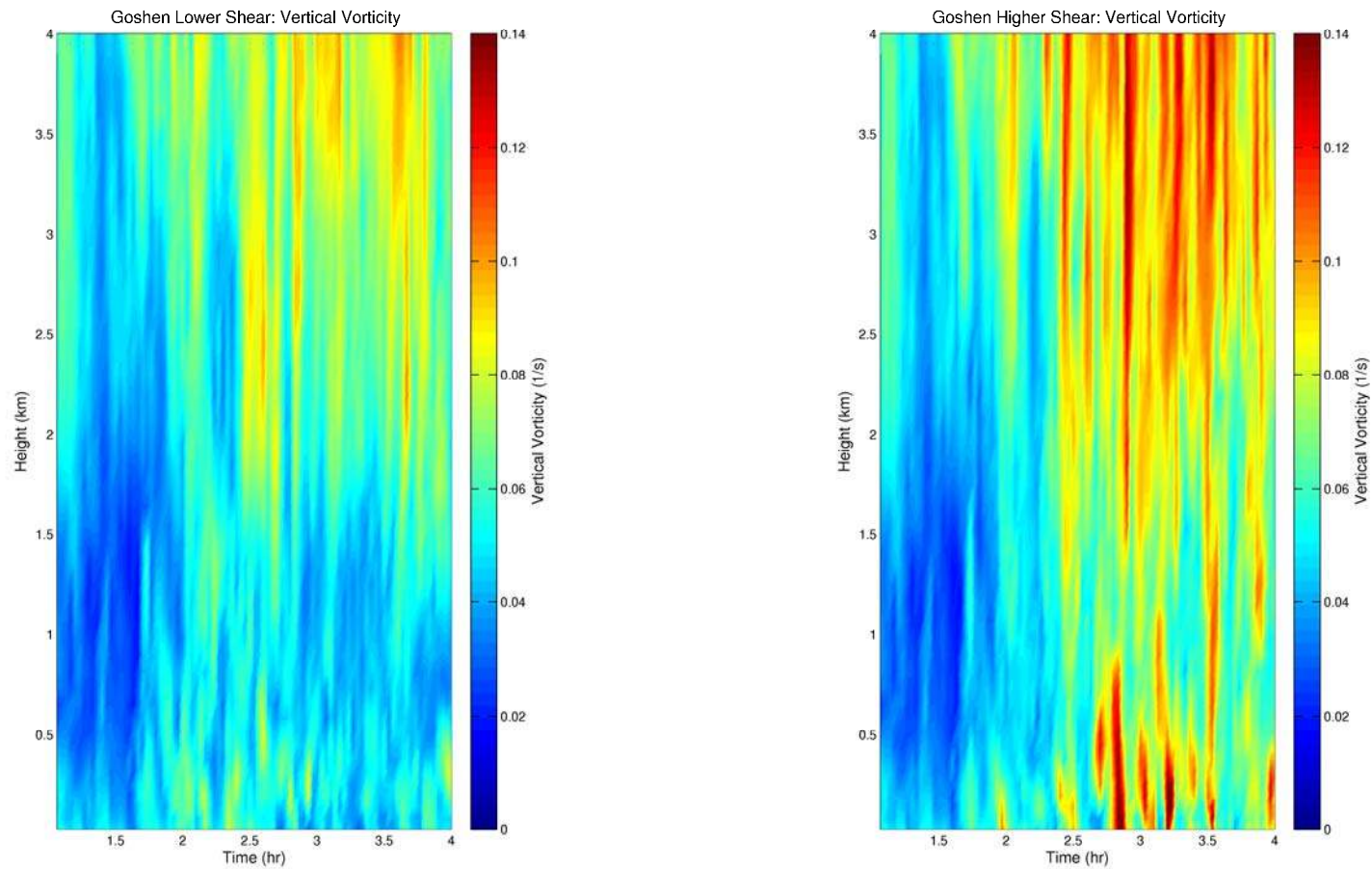
Figure 3.3 Time height plot of the maximum vertical vorticity (1/s) in a 50 x 50 km box following the supercell's mesocyclone for both the lower shear Goshen Control simulation (left) and the higher shear Goshen BSS simulation (right). The BSS process begins at 1.5 hr.
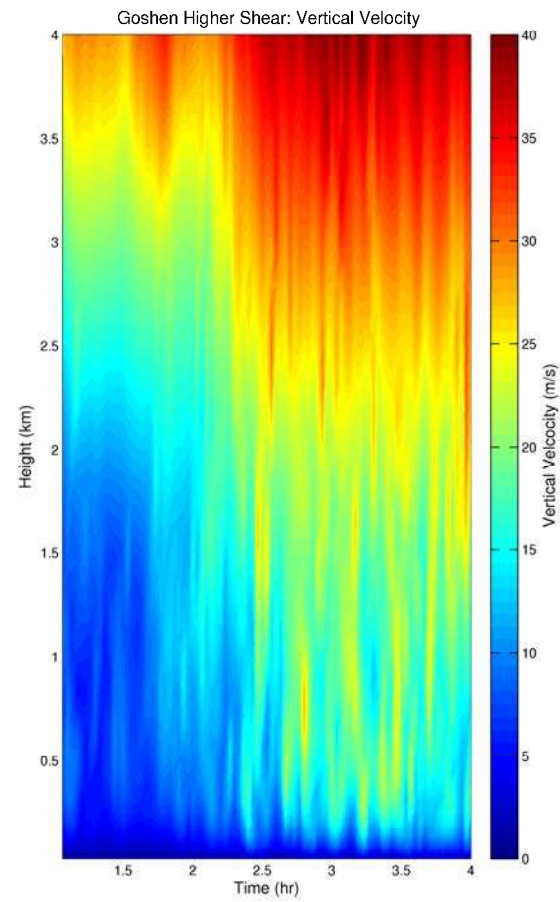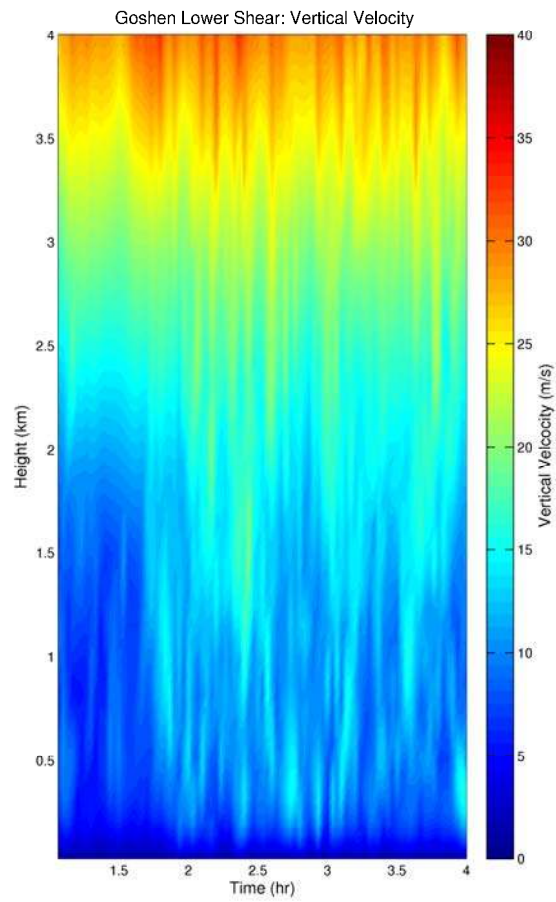
Figure 3.4: As in Figure 3.3, except displayed is the maximum vertical velocity (m/s). The BSS process begins at 1.5 hr.
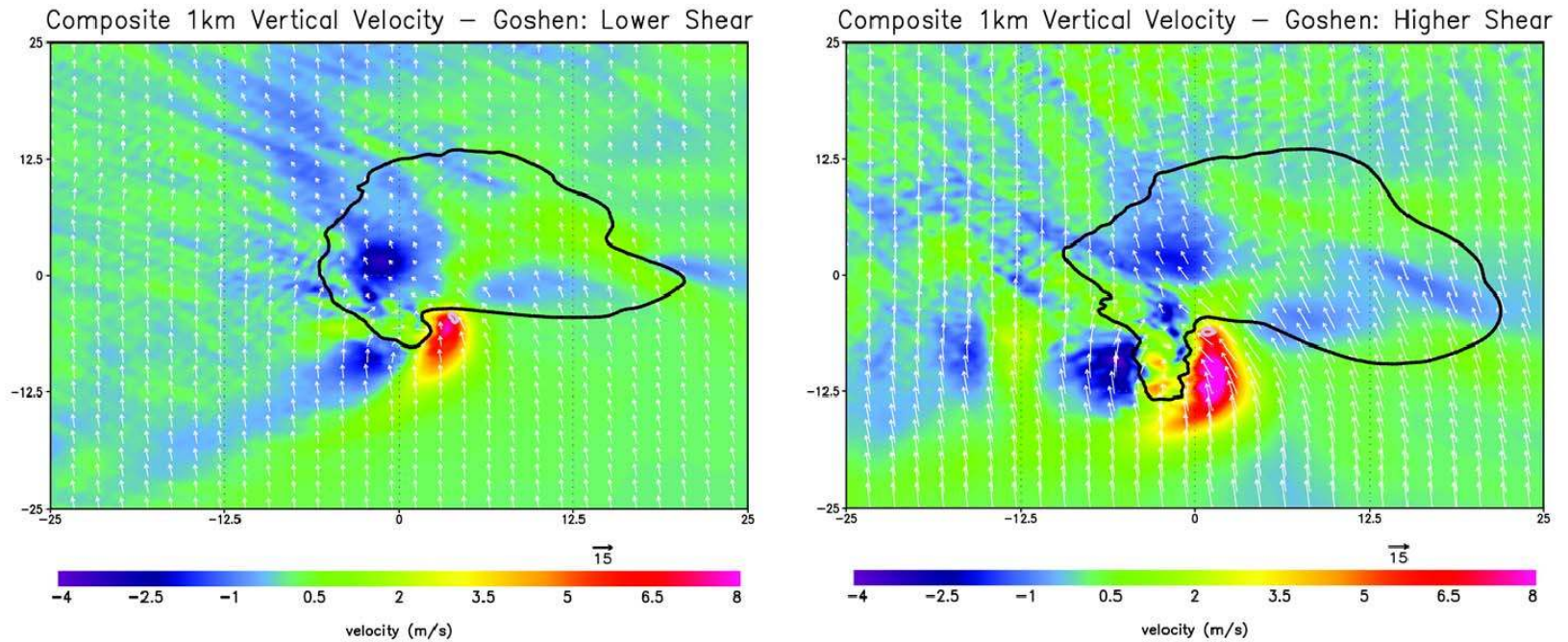
Figure 3.5: Time composite plot showing the average spatial 1 km vertical velocity field (m/s) for the hour following the end of the BSS process for the lower shear Goshen Control (left) and the higher shear Goshen BSS simulation (right). The 20 dbz composite reflectivity contour is shown in black. The 0.005 s^{-1} composite surface vertical vorticity contour is shown in gray. Composite, ground-relative 1 km wind vectors are shown in white. Time composite plots were calculated by averaging values in a 50 x 50 km box following the supercell's mesocyclone (determined by the maximum 2-5 km updraft helicity; Kain et al. 2008).
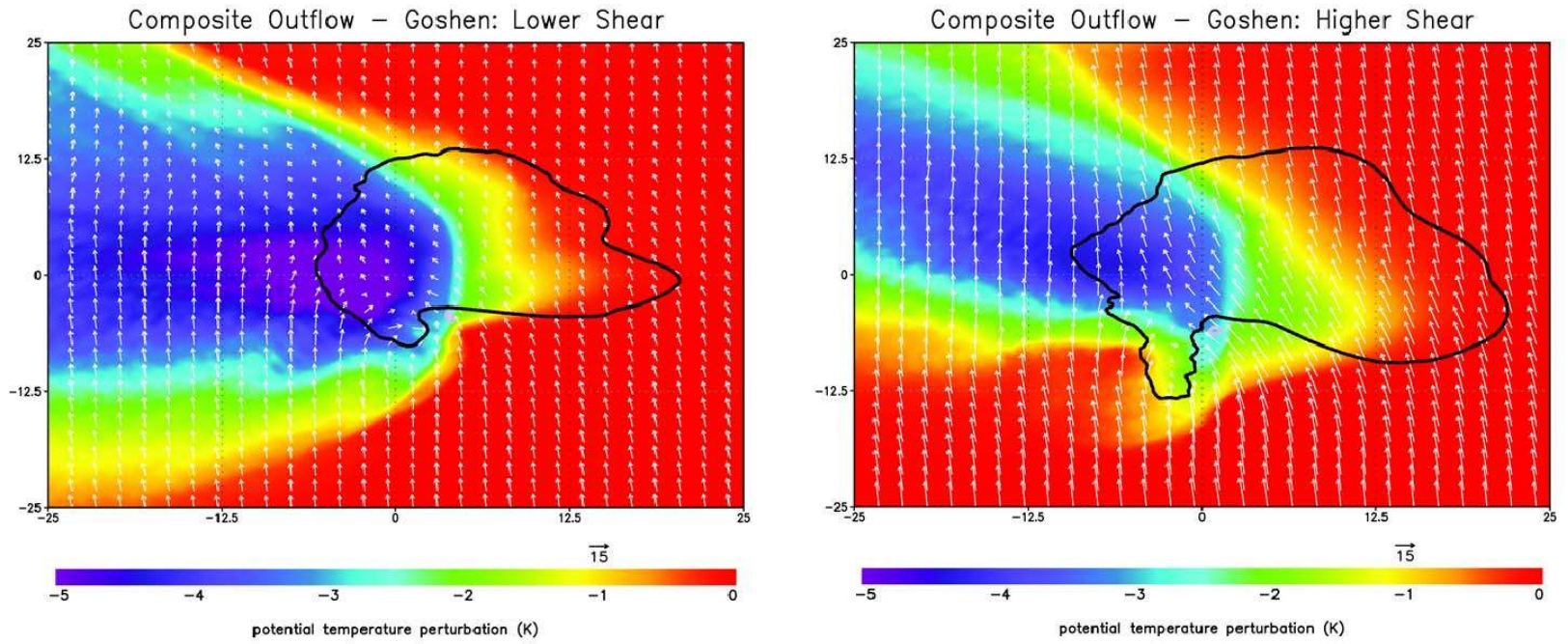
Figure 3.6: As in Figure 3.5, except displayed is the surface potential temperature perturbation (K).
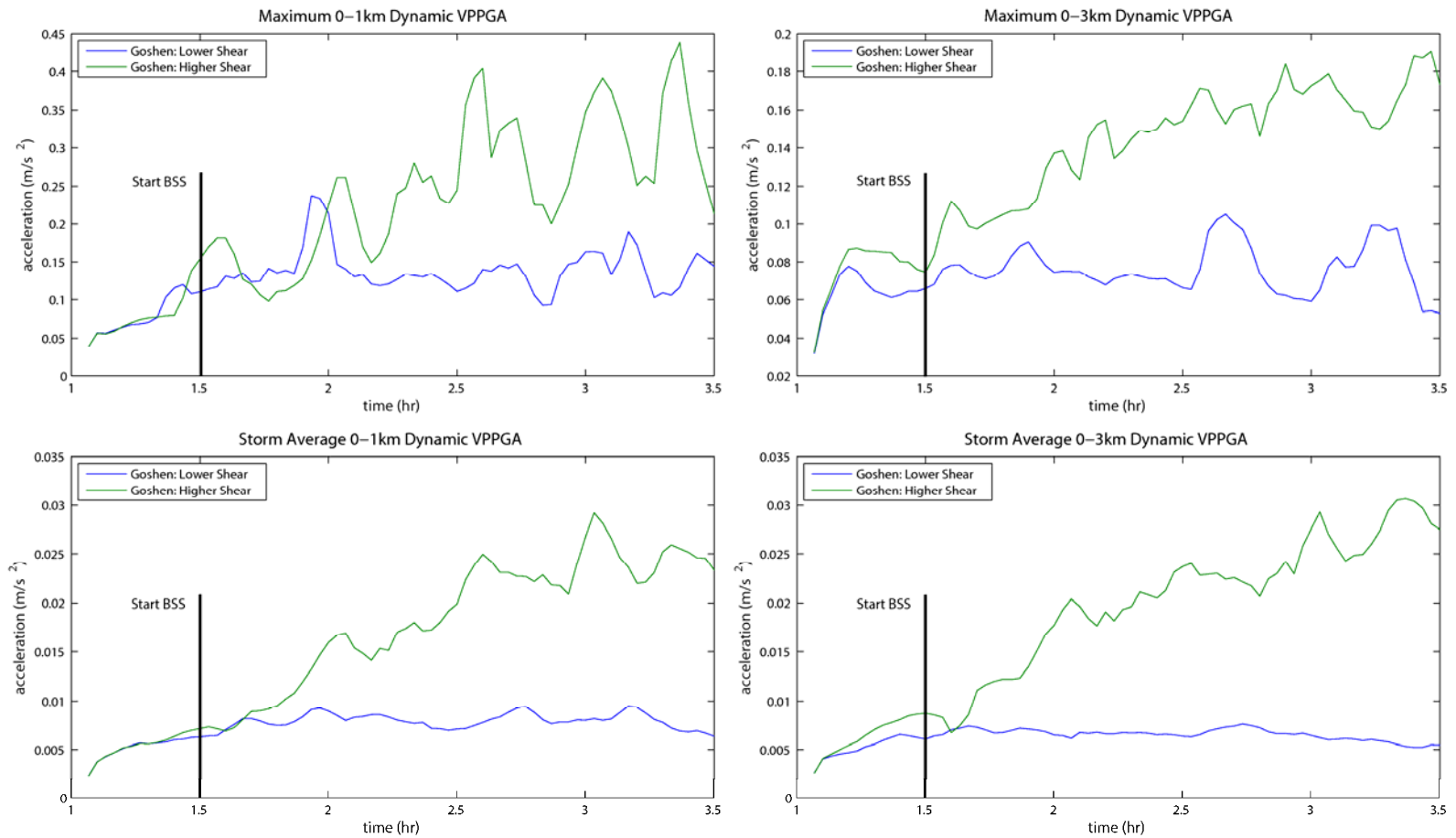
Figure 3.7: Time series comparing dynamic VPPGA (m/s^2) for both the lower shear Goshen Control and the higher shear Goshen BSS supercells. Top panels show the maximum acceleration value for both the 0-1 and 0-3 km layers in a 50 x 50 km box following the supercell's mesocyclone. The bottom panels are similar to the top panels, except displayed is the storm averaged acceleration in the 50 x 50 km box.
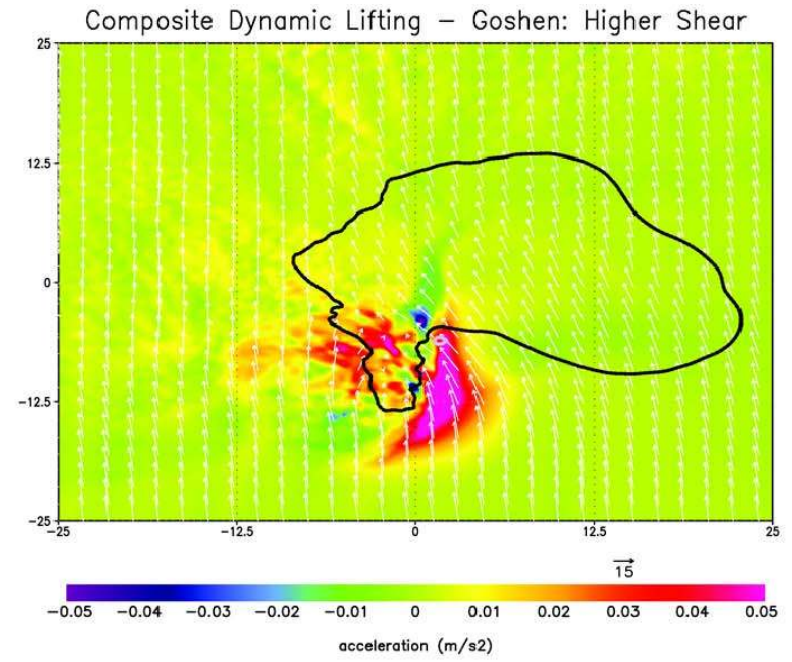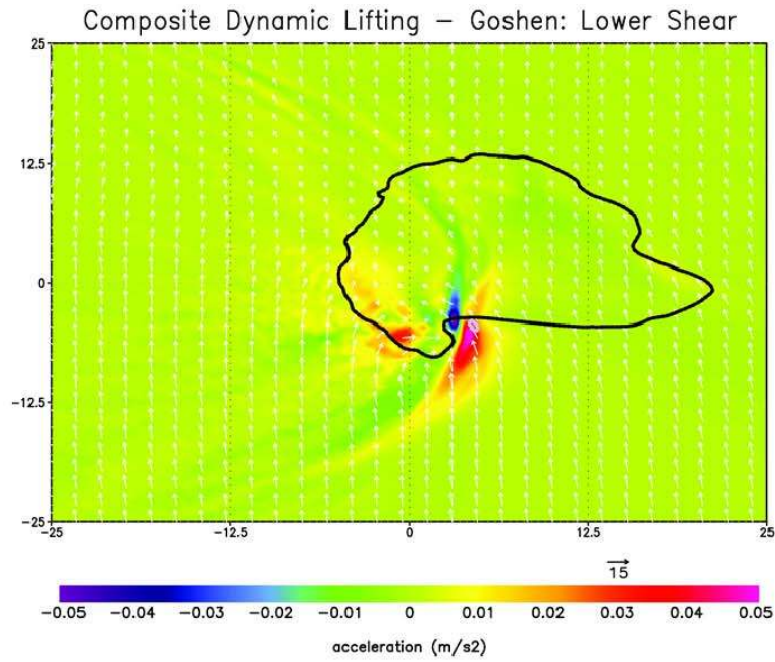
Figure 3.8: As in Figure 3.5, except displayed is the 0-1 km dynamic VPPGA (m/s^2).
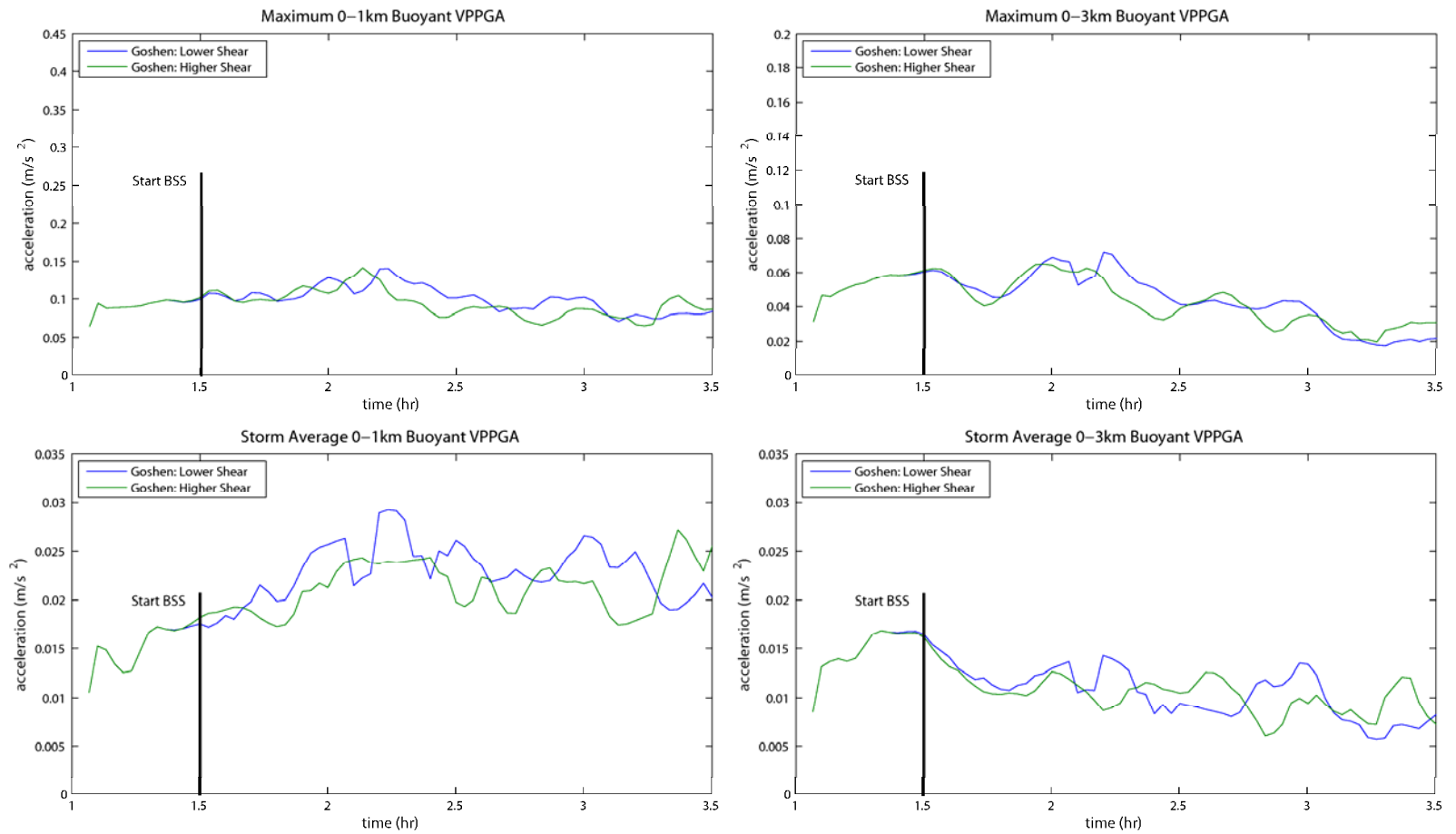
Figure 3.9: As in Figure 3.7, except displayed is the buoyant VPPGA (m/s^2).
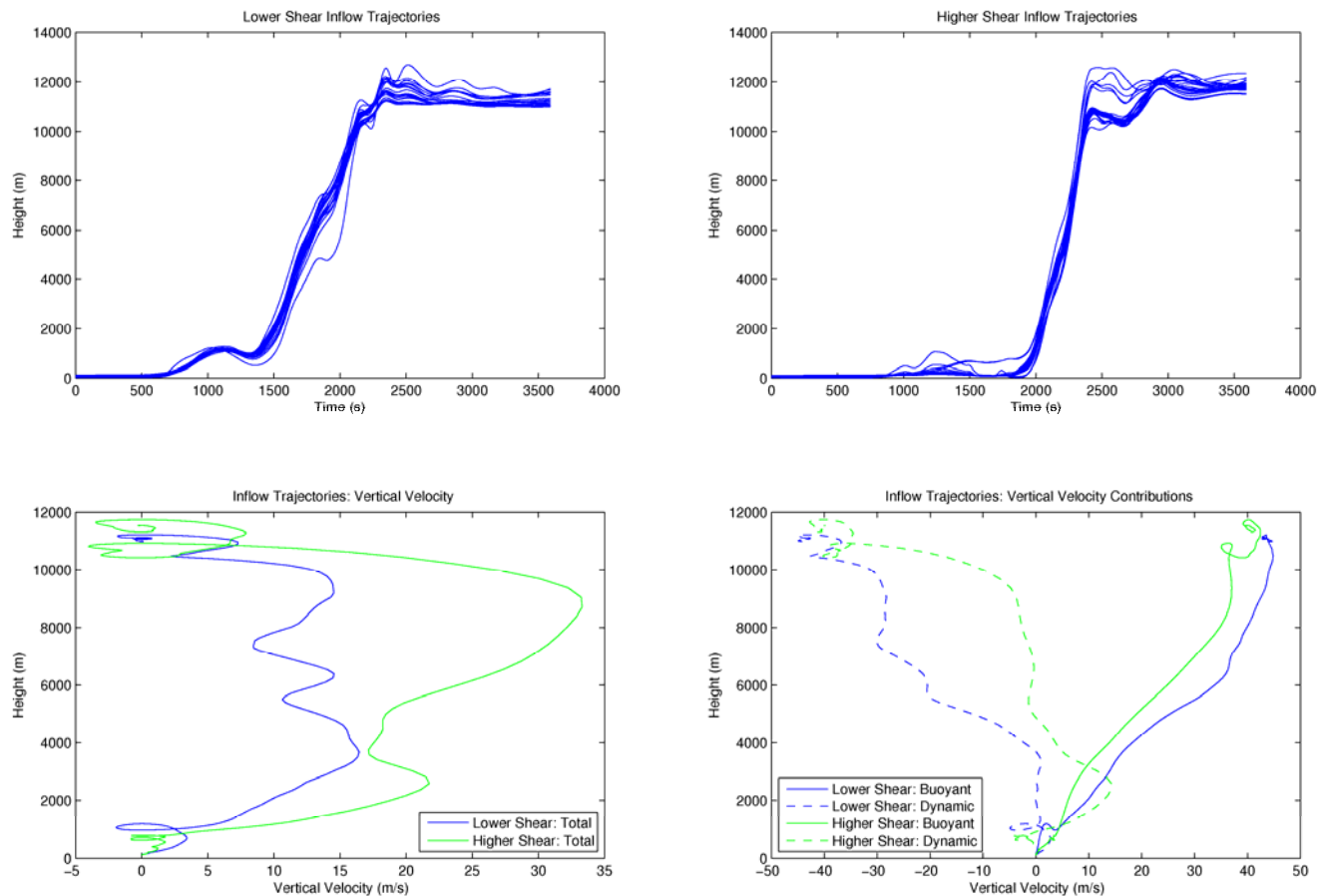
Figure 3.10: The top panels show the time series of altitude for the 20 inflow trajectories in both the lower shear Goshen Control supercell (left) and the higher shear supercell Goshen BSS supercell (right). The bottom left panel shows the composite total vertical velocity with respect to height along the 20 inflow trajectories in both the lower shear Goshen Control supercell (blue) and the higher shear supercell Goshen BSS supercell (green). The bottom right panels shows the composite buoyant and dynamic contributions to the total vertical velocity in both the lower shear Goshen Control supercell (blue) and the higher shear supercell Goshen BSS supercell (green).

Figure 3.11: Box plot showing the maximum height (m; left), vertical velocity (m/s; center), and maximum vertical velocity stretching ($1/s^2$; right) for outflow trajectories of both the lower shear Goshen Control and higher shear Goshen BSS supercell. All trajectories acquired at least 0.03 s^{-1} vertical vorticity and a -2.5 K potential temperature perturbation at the bottom model level. Trajectories were filtered to have the same initial buoyancy.
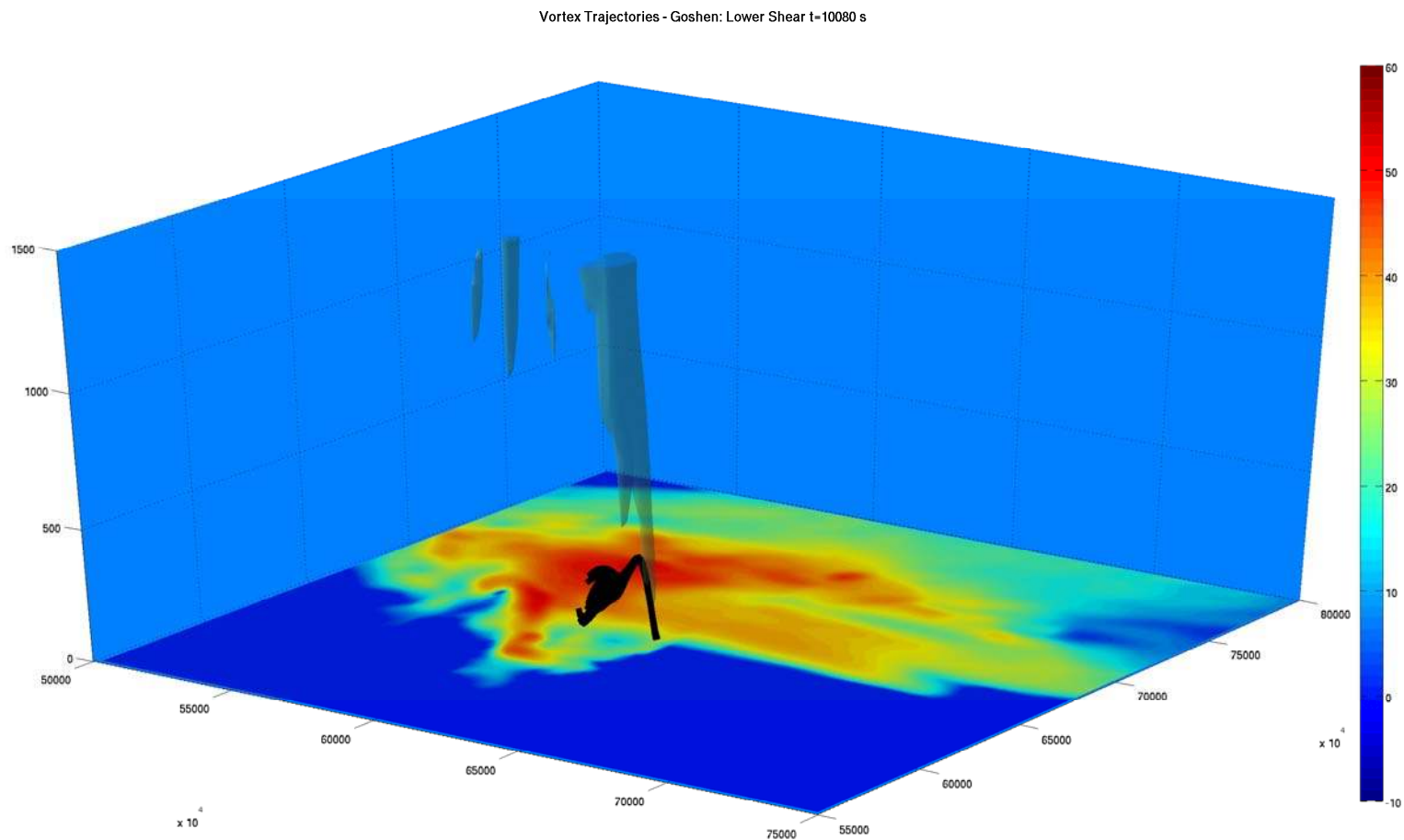
Figure 3.12: Three-dimensional view of the low-level updraft, near-surface reflectivity field, and the 20 near-vortex trajectories that acquired the most surface vorticity at the bottom model level in the lower shear Goshen Control supercell. Shaded on the surface is the model simulated base reflectivity (~dbz). Updraft isosurfaces of 9 and 18 m/s are shown light green and light red, respectively.
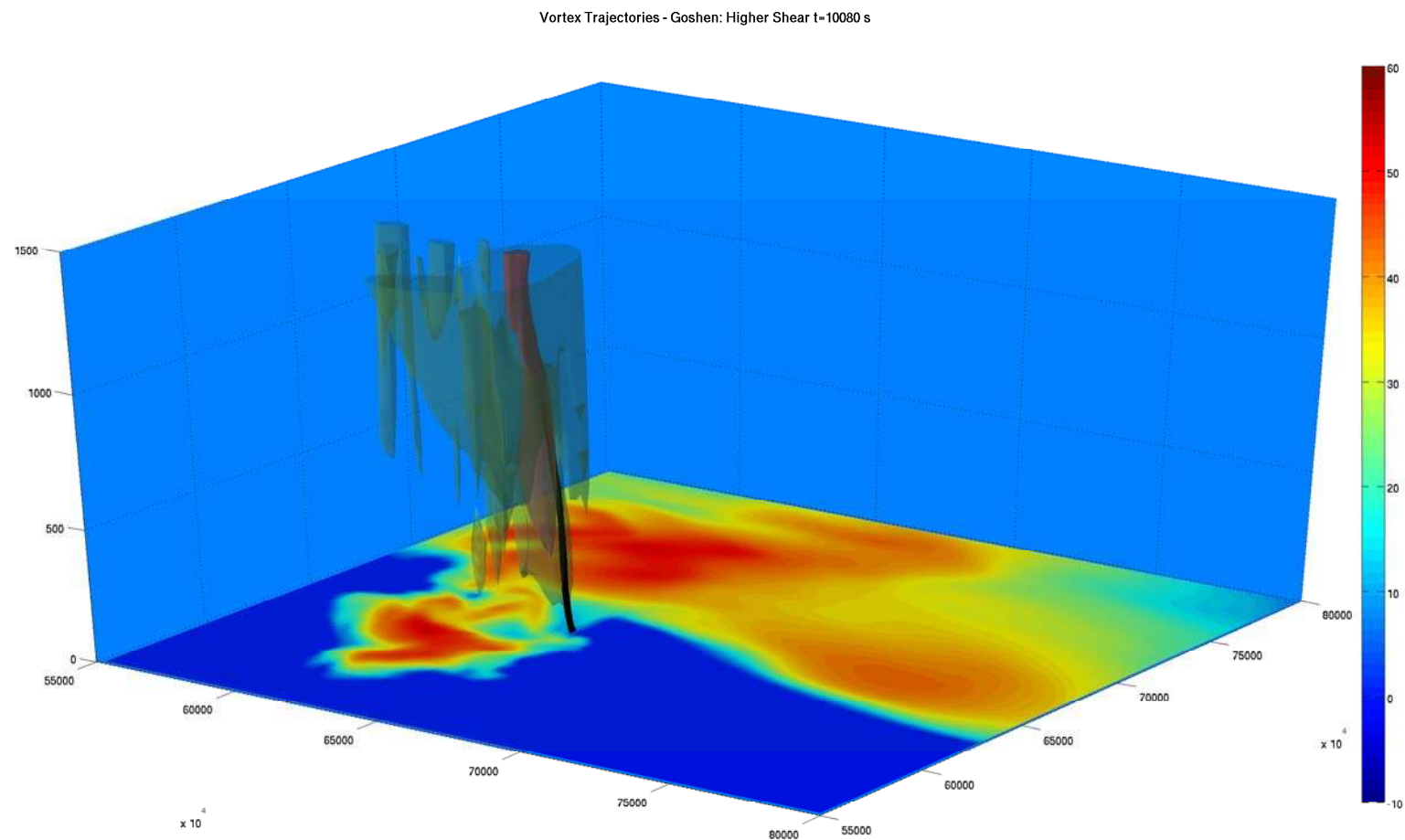
Figure 3.13: As in Figure 3.12, except displayed is the higher shear Goshen BSS supercell.
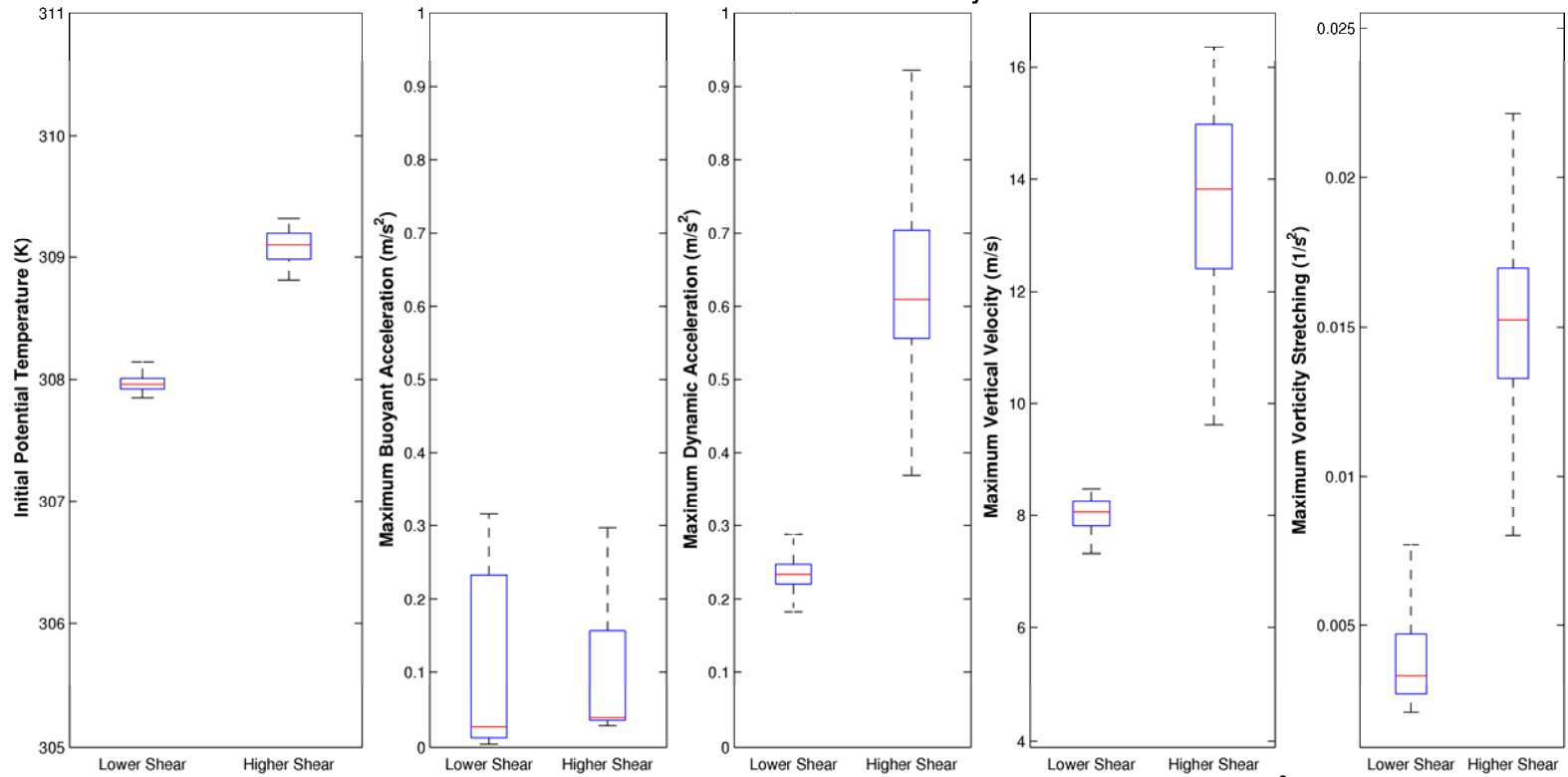
Figure 3.14: Box plot showing the initial potential temperature (K), mean buoyant acceleration (m/s^2), mean dynamic acceleration (m/s^2), mean vertical velocity, and mean stretching of vertical vorticity (1/s^2) for the 20 near-vortex trajectories that acquired the most surface vorticity at the bottom model level in the lower shear Goshen Control and higher shear Goshen BSS supercell.
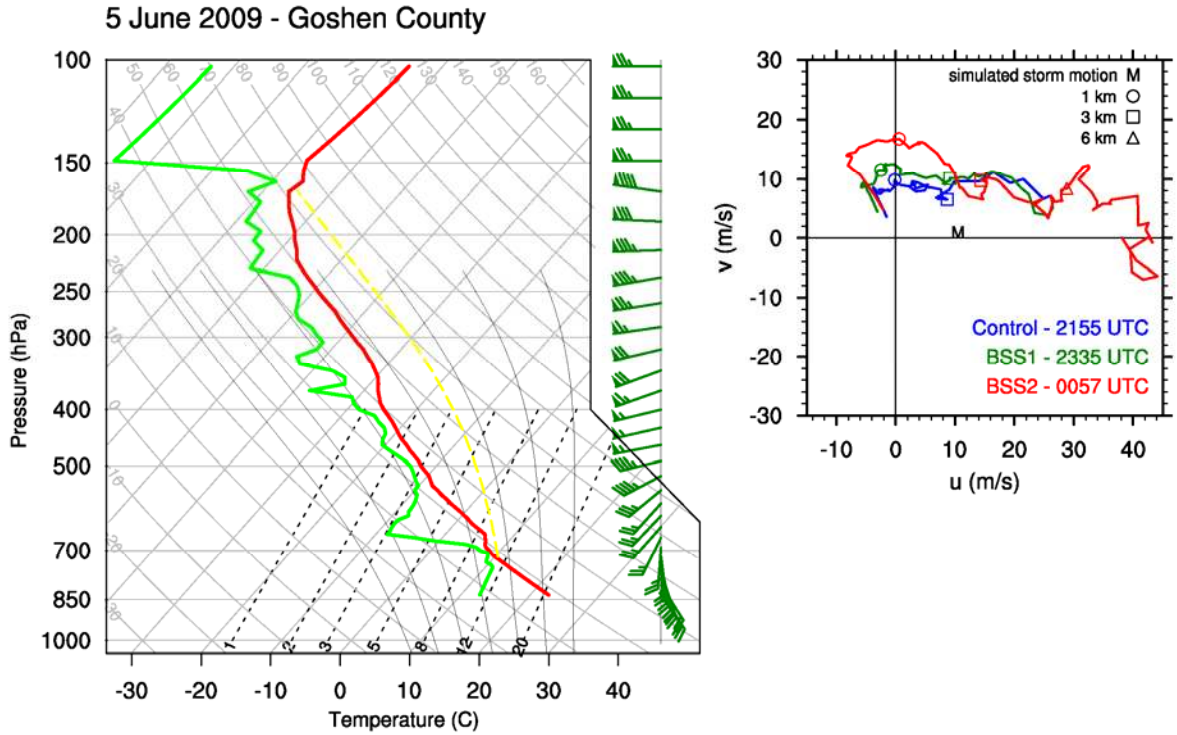
Figure 3.15: As in Figure 2.1, except displayed is the 2335 UTC thermodynamics for the 05 June 20009 "Goshen County" Tornadic Supercell.
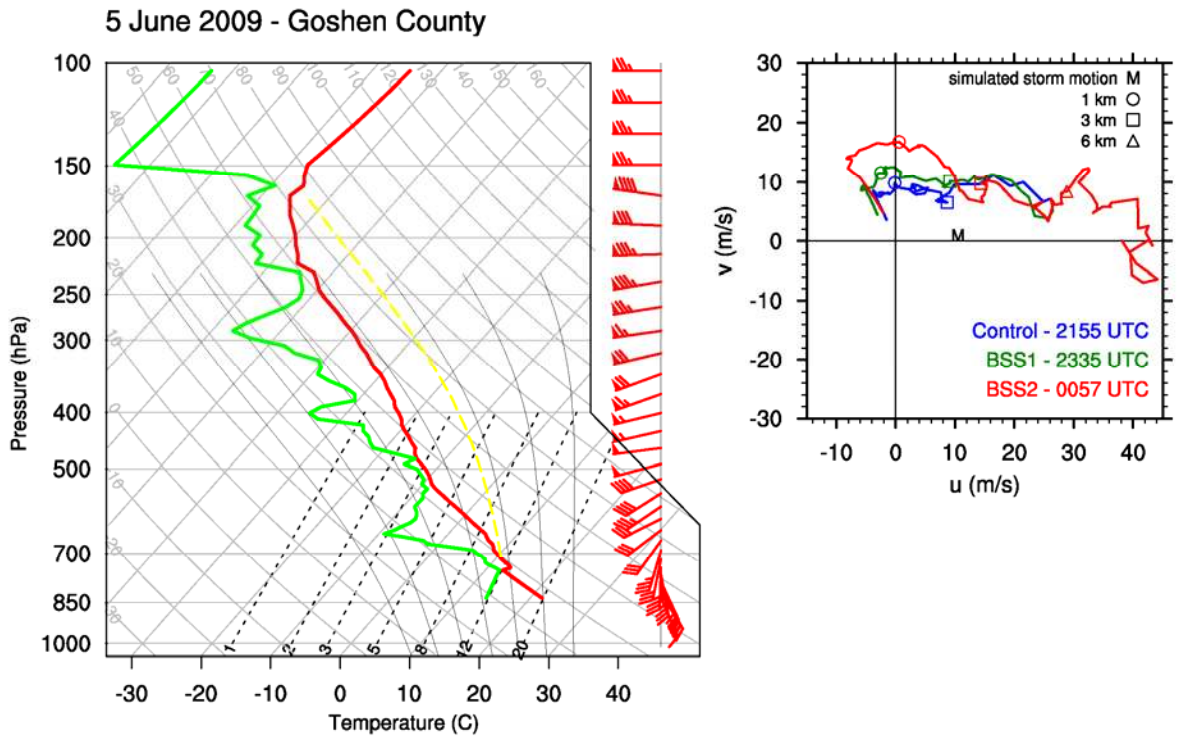
Figure 3.16: As in Figure 2.1, except displayed is the 0057 UTC thermodynamics for the 05 June 20009 "Goshen County" Tornadic Supercell.
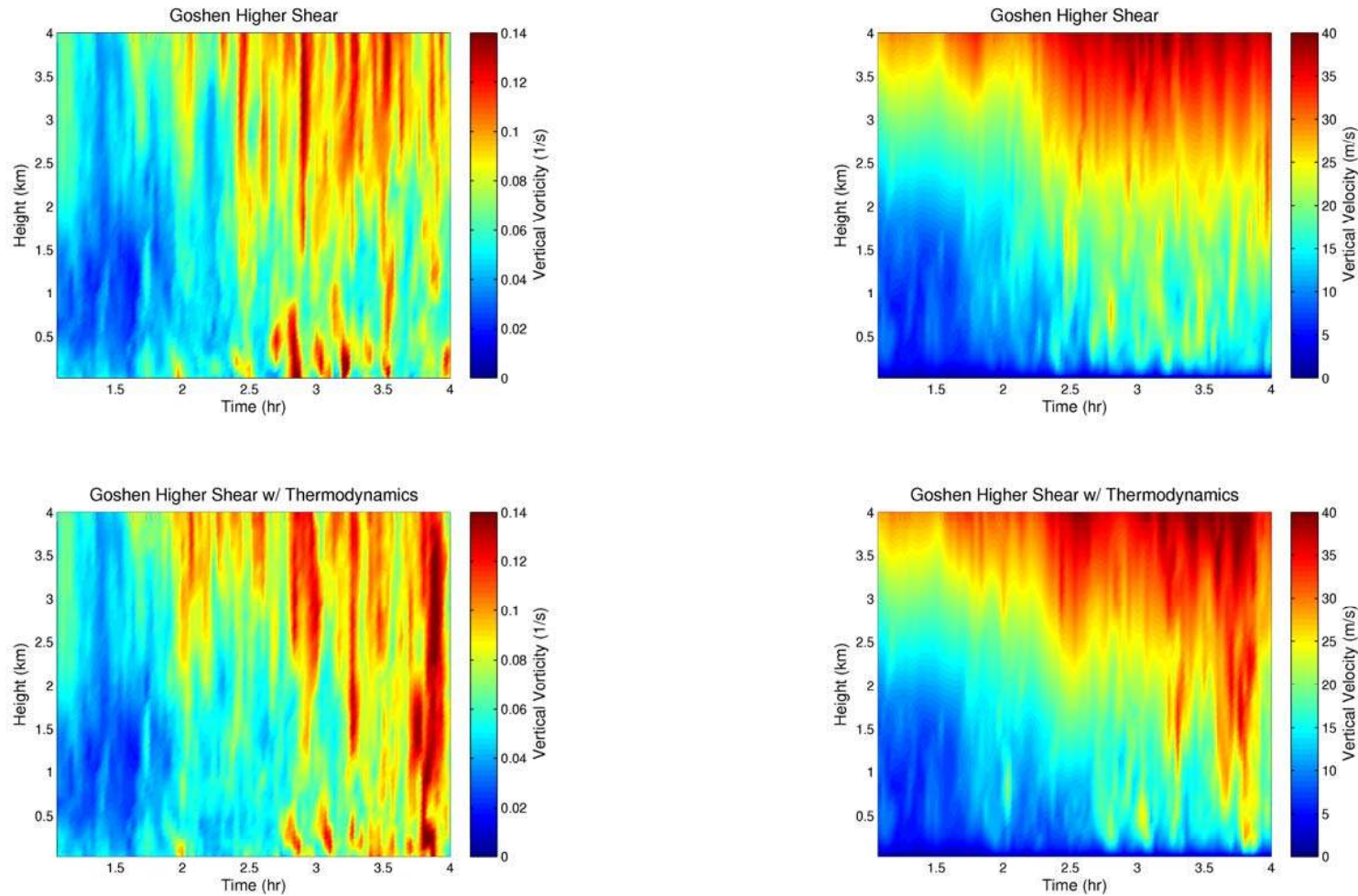
Figure 3.17: Time height plot of (left) the maximum vertical vorticity (1/s) and (right) the maximum vertical velocity (m/s) in a 50 x 50 km box following the supercell's mesocyclone for both the higher shear Goshen BSS (top) and the higher shear Goshen BSS with thermodynamics (bottom). The BSS process begins at 1.5 hr.
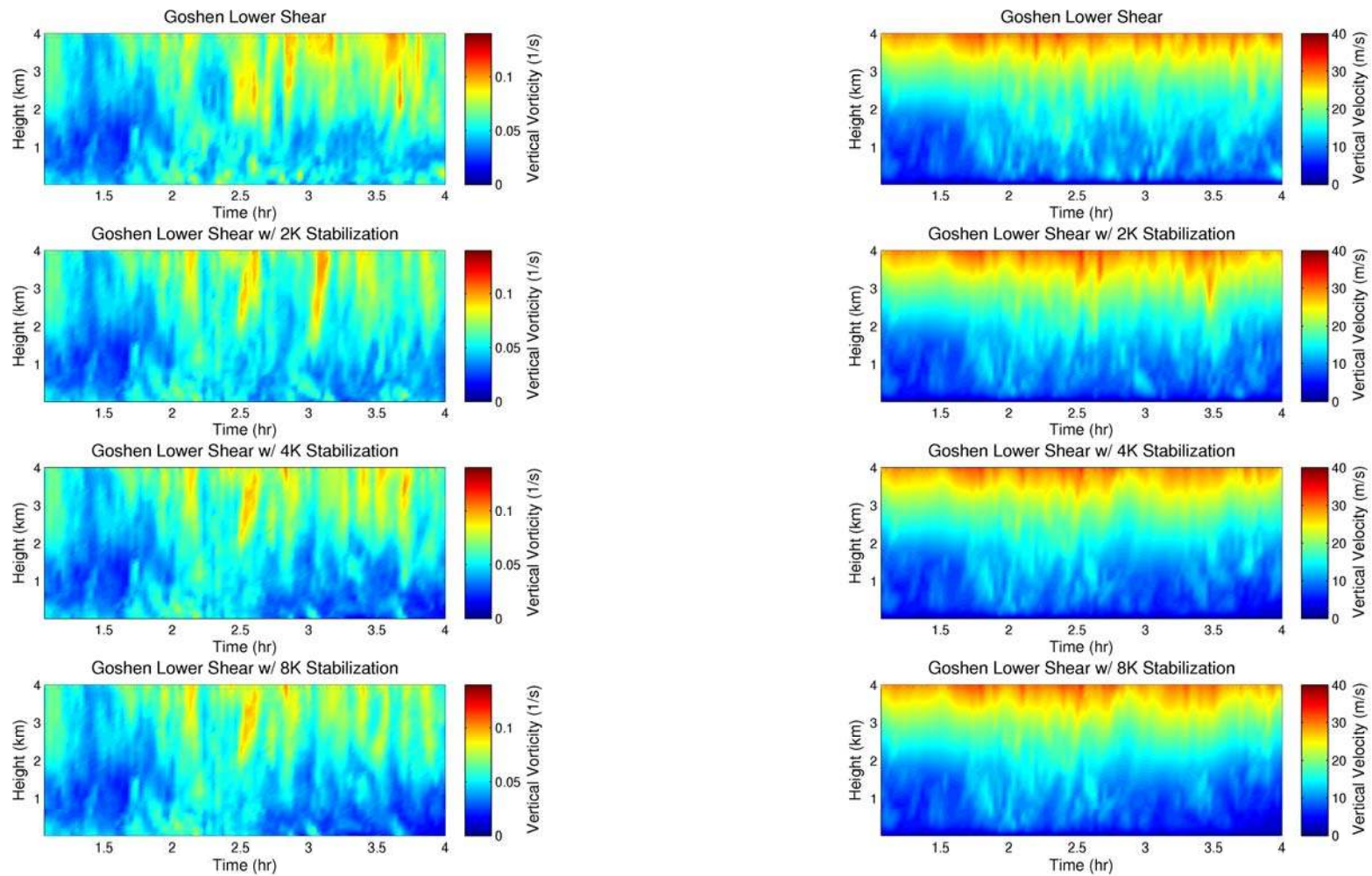
Figure 3.18: Time height plot of (left) the maximum vertical vorticity (1/s) and (right) the maximum vertical velocity in a 50 x 50 km box following the supercell's mesocyclone for the lower shear Goshen Control (top row) and the lower shear Goshen Control with 2, 4, and 8 K stabilization simulations (bottom three rows, respectively). The BSS process begins at 1.5 hr.
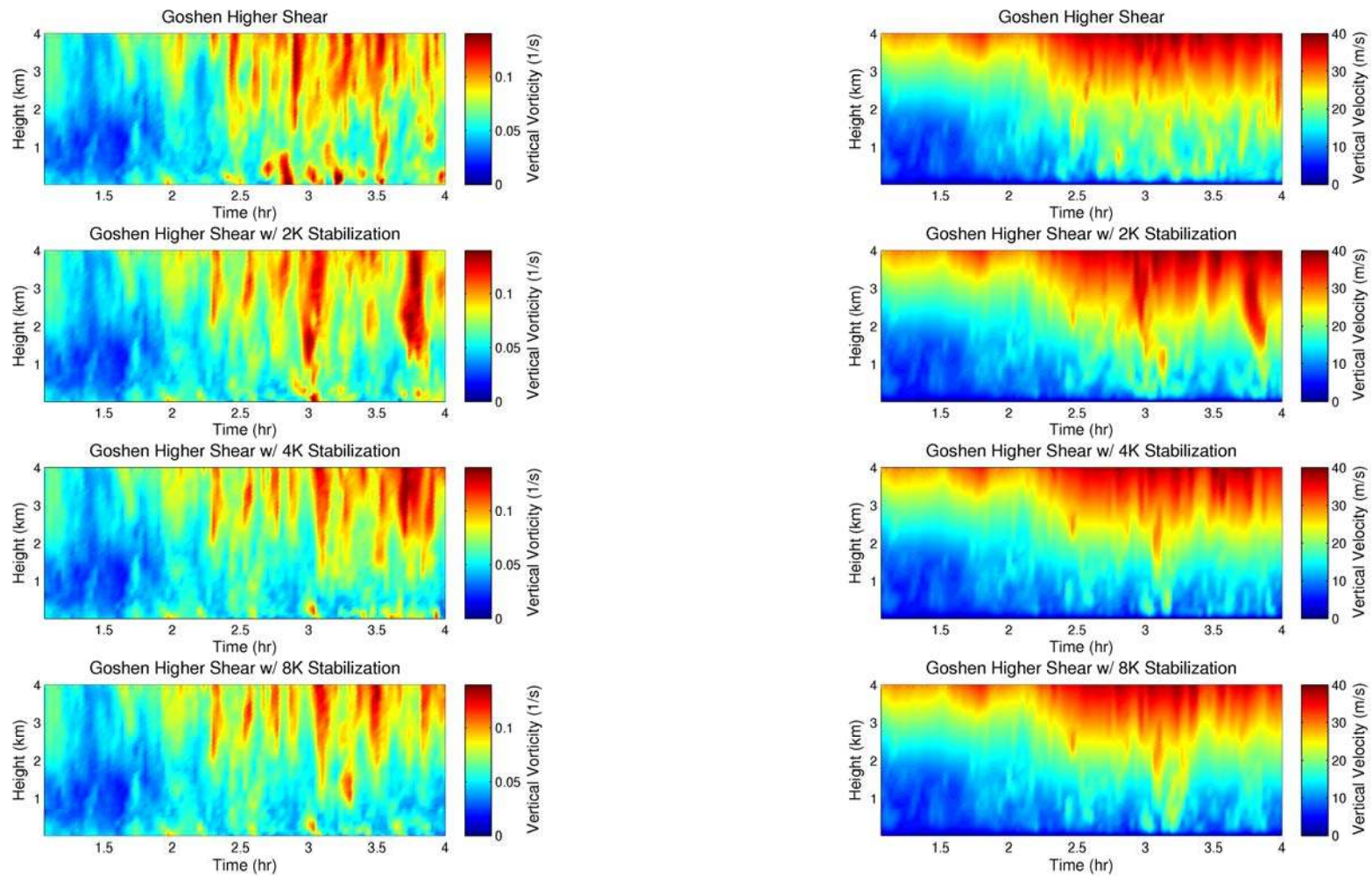
Figure 3.19: As in Figure 3.18, except for the higher shear Goshen BSS (top row) and the higher shear Goshen BSS with 2, 4, and 8 K stabilization simulations (bottom three rows, respectively).

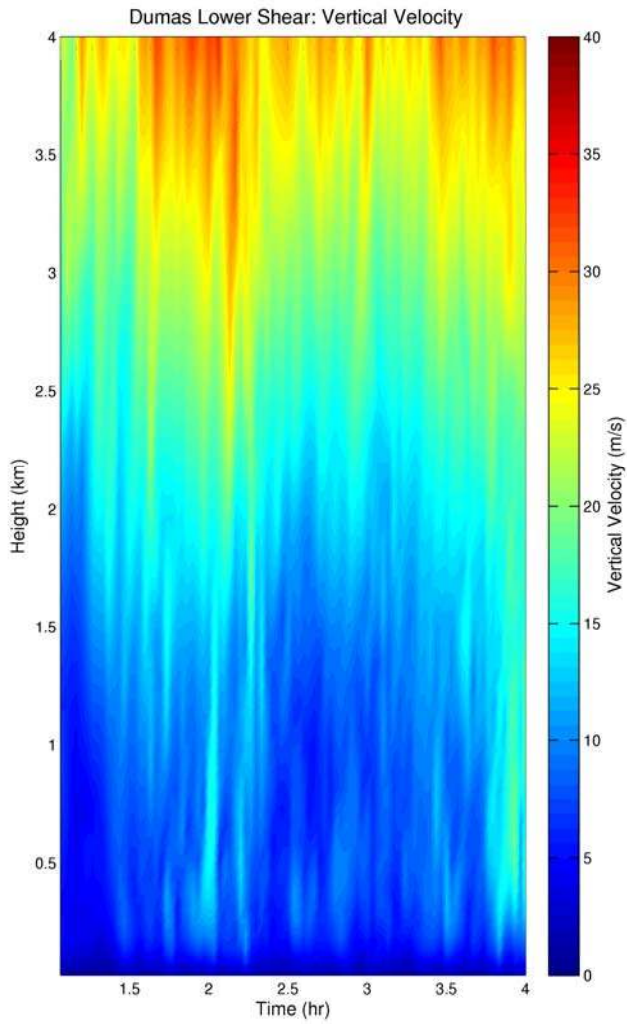Figure 4.1: As in Figure 3.1, except for the 18 May 2010 "Dumas, Texas" case.
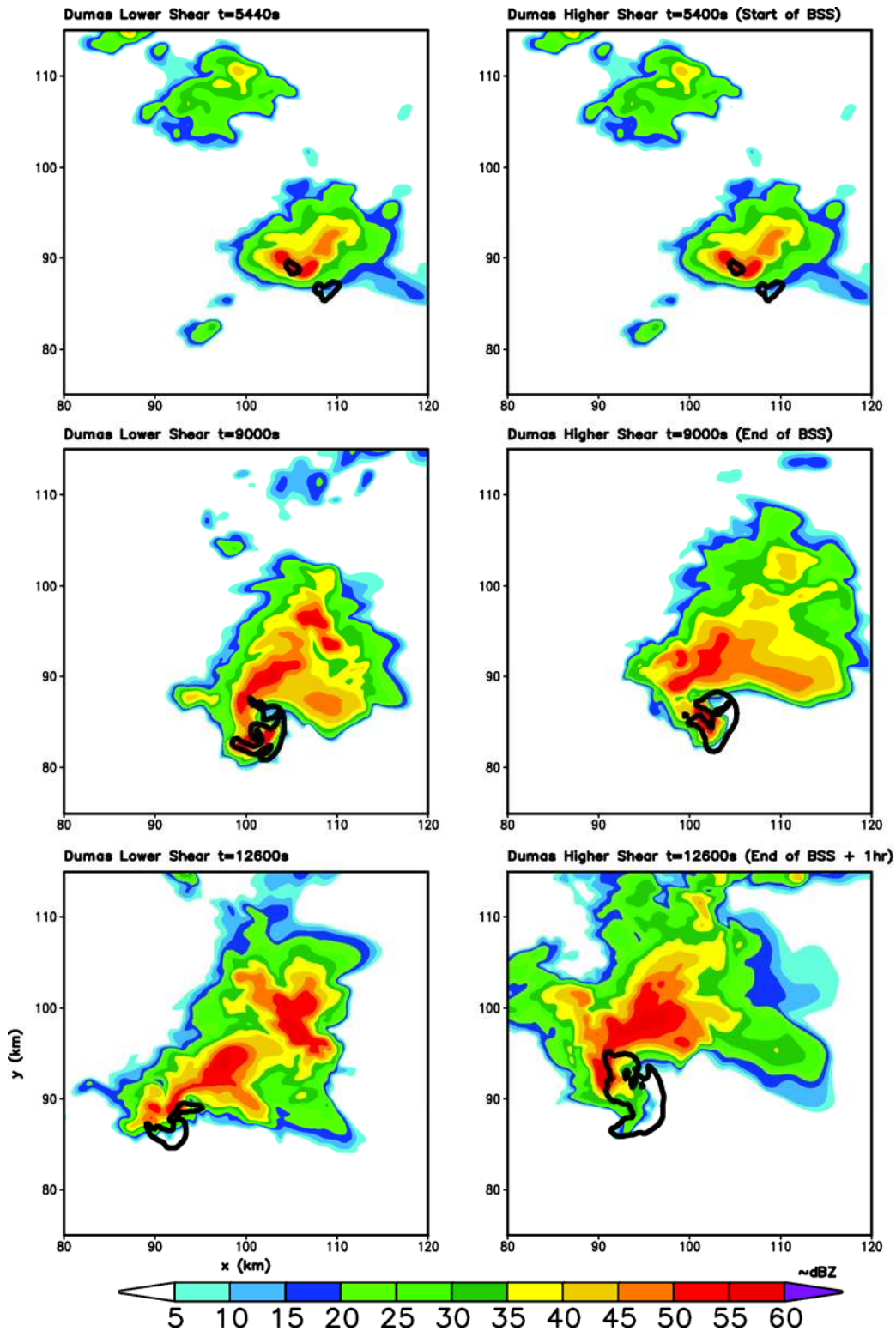
Figure 4.2: As in Figure 3.2, except for the lower shear Dumas Control simulation (left) and the higher shear Dumas BSS simulation (right).
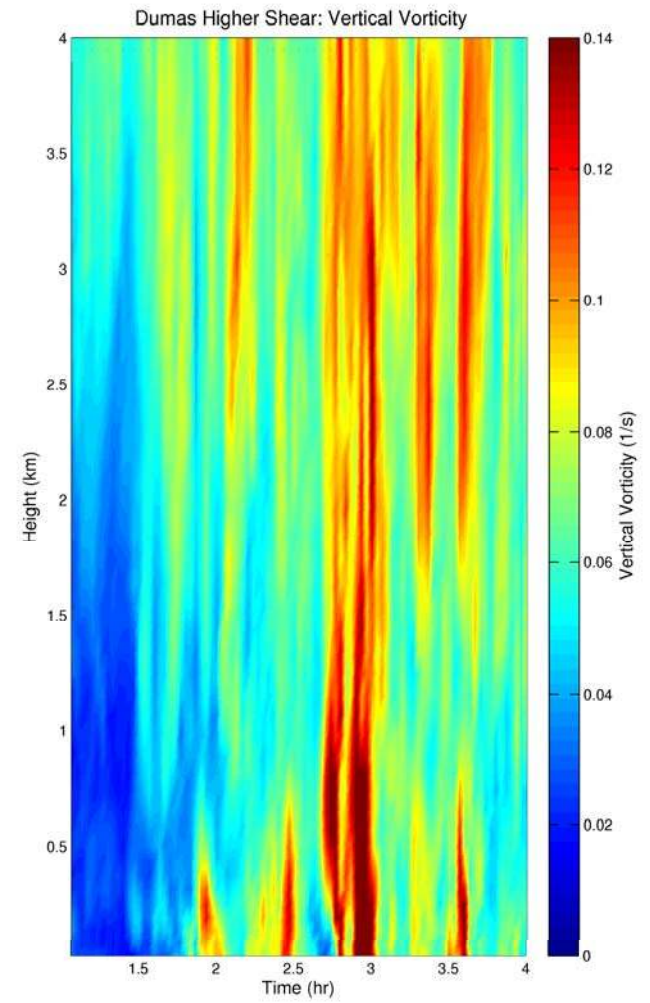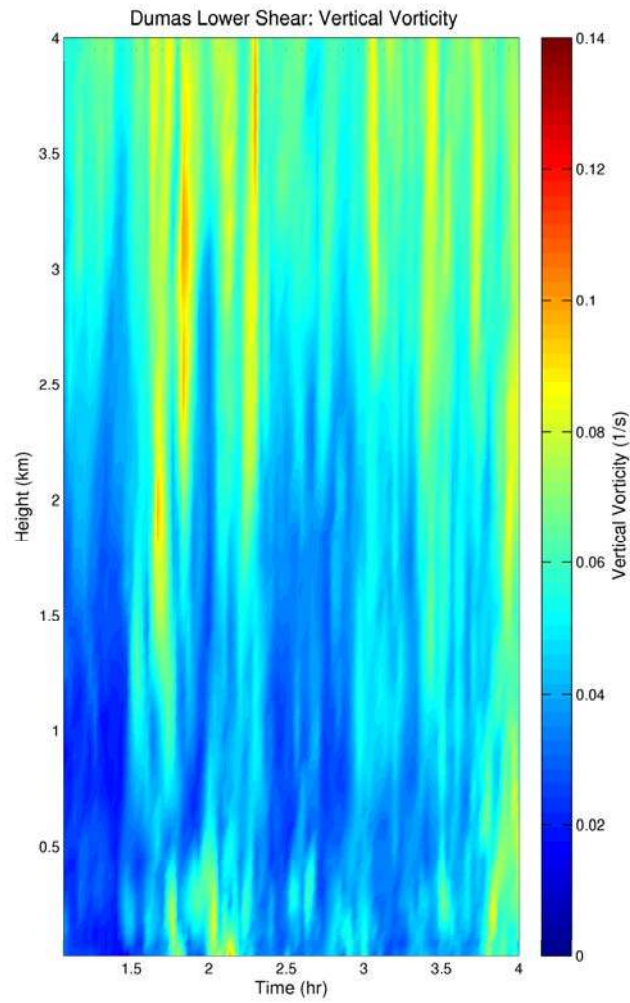
Figure 4.3: As in Figure 3.3, except for the lower shear Dumas Control simulation (left) and the higher shear Dumas BSS simulation (right).
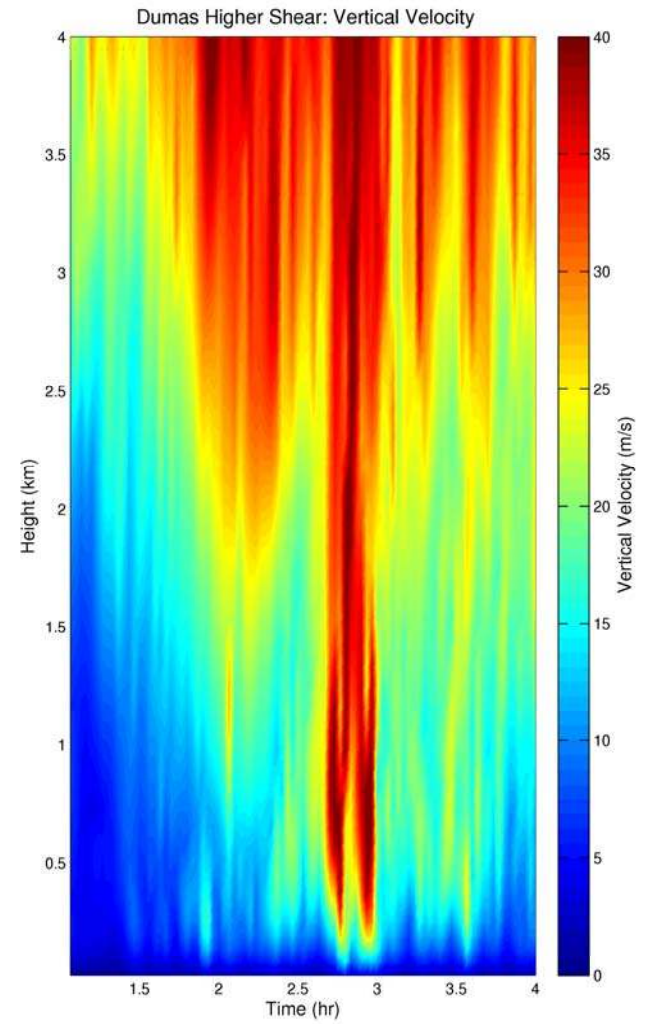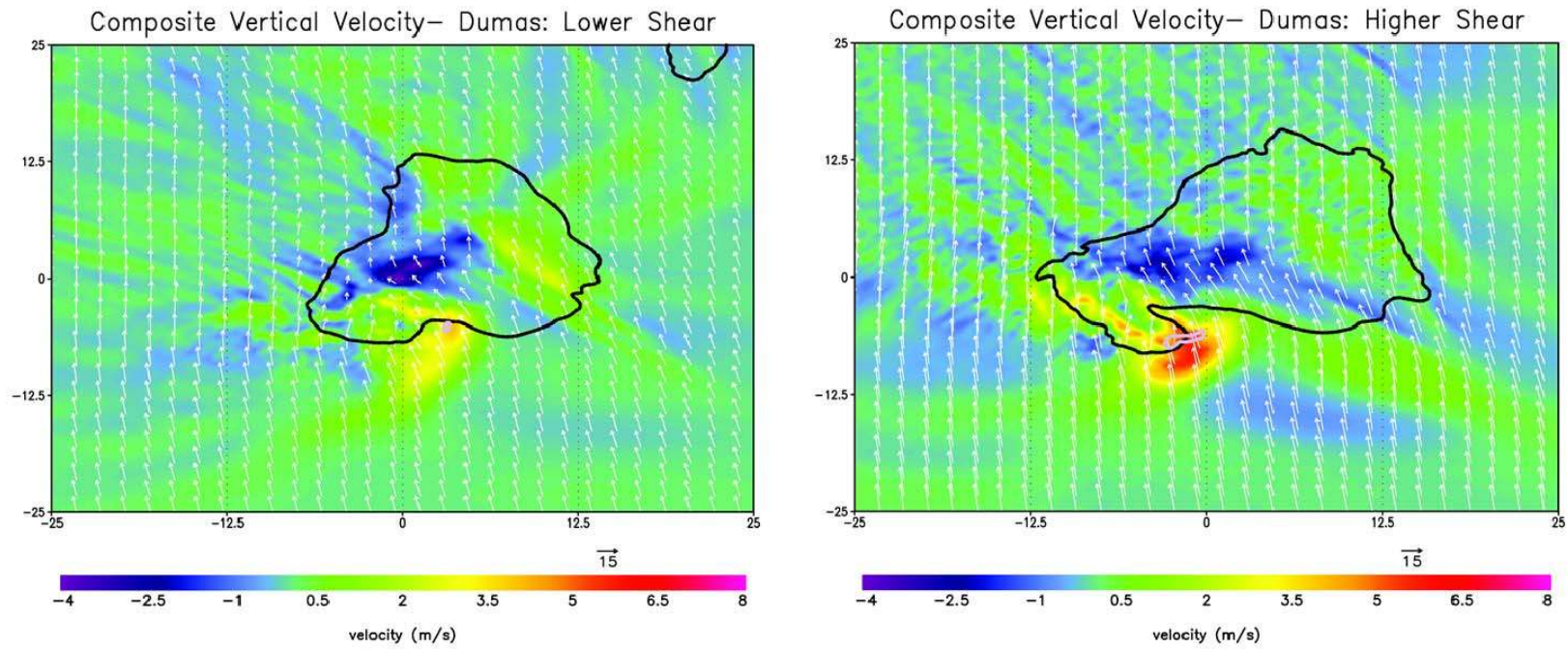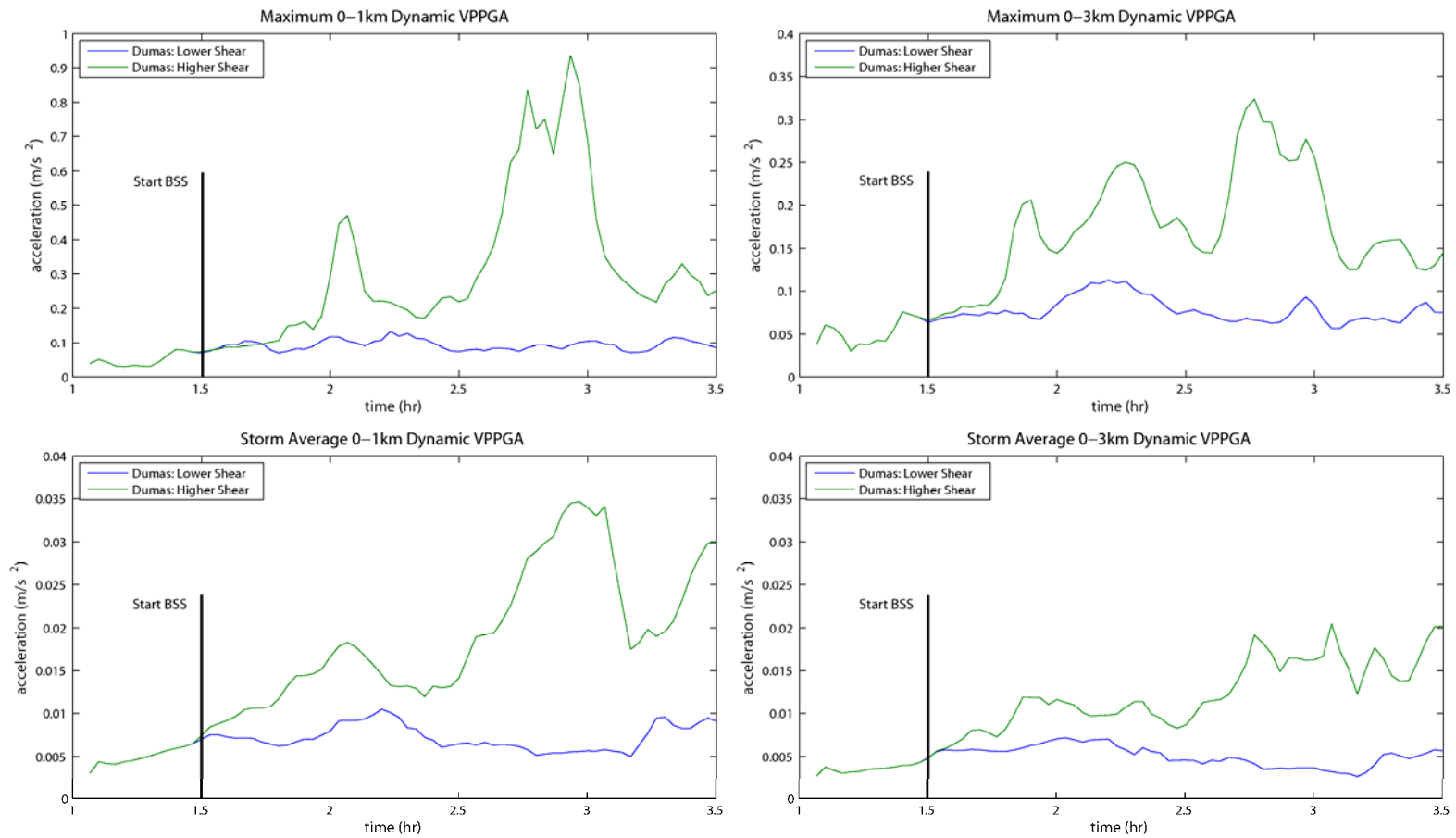
Figure 4.4: As in Figure 3.4, except for the lower shear Dumas Control simulation (left) and the higher shear Dumas BSS simulation (right).

Figure 4.5: As in Figure 3.5, except for the lower shear Dumas Control simulation (left) and the higher shear Dumas BSS simulation (right).

Figure 4.6: As in Figure 3.7, except for the lower shear Dumas Control and the higher shear Dumas BSS supercells.
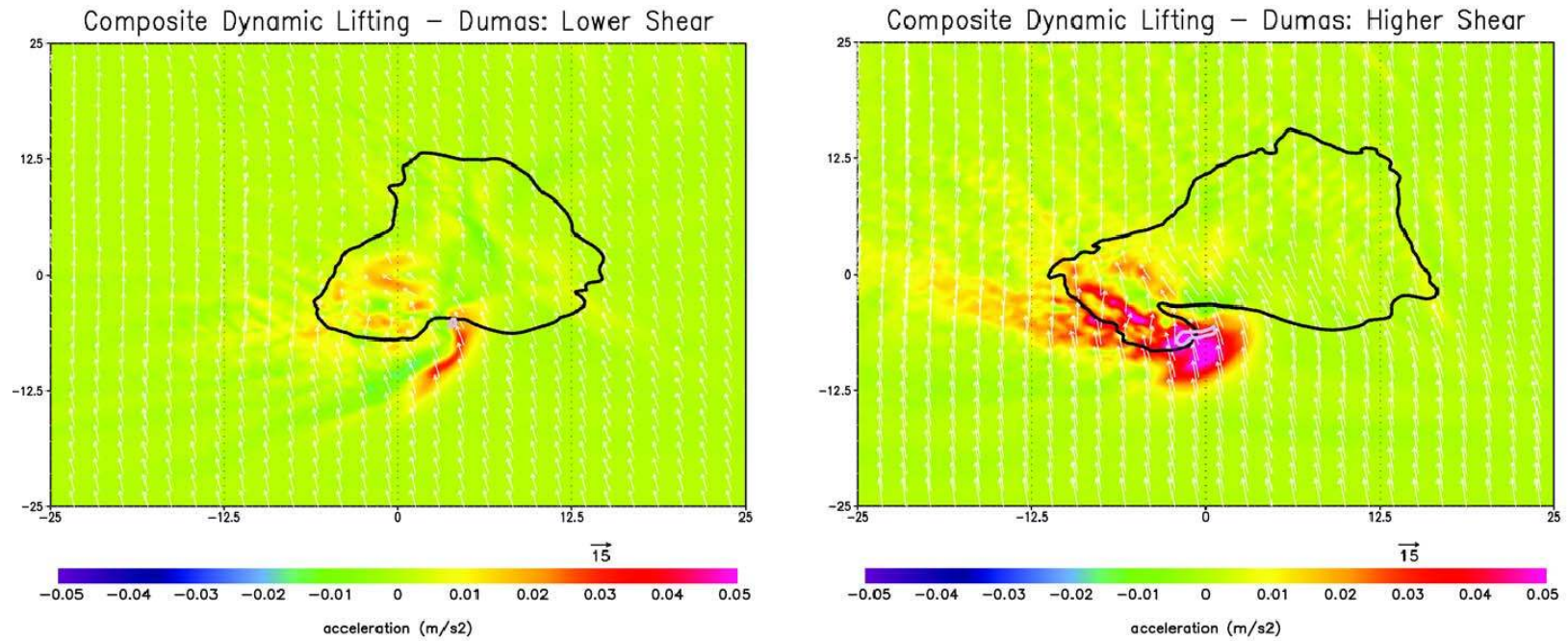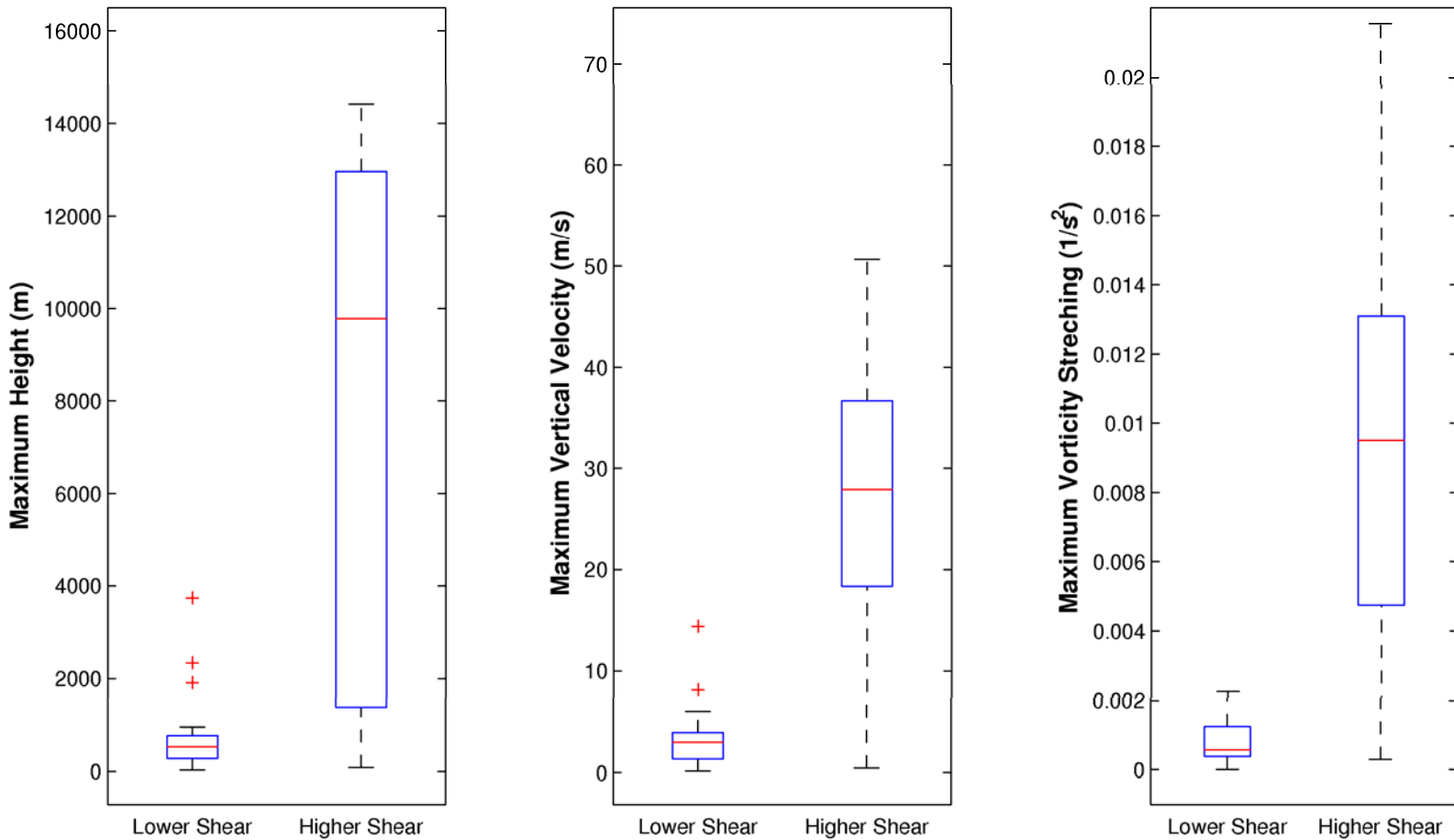
Figure 4.7: As in Figure 3.8, except for the lower shear Dumas Control simulation (left) and the higher shear Dumas BSS simulation (right).

Figure 4.8: As in Figure 3.11, except for the lower shear Dumas Control and the higher shear Dumas BSS supercells
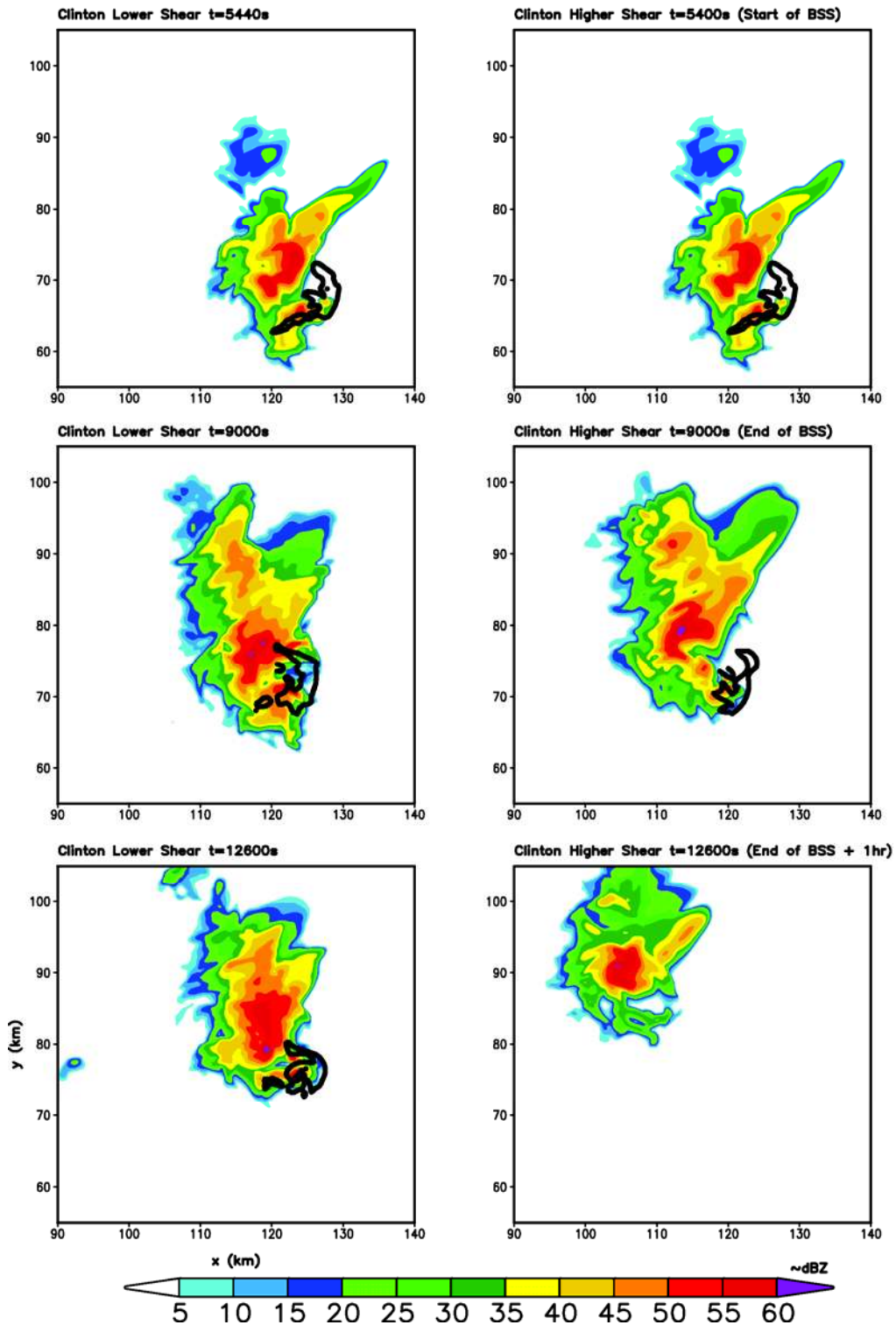
Figure 5.1: As in Figure 3.2, except for the lower shear Clinton Control simulation (left) and the higher shear Clinton BSS simulation (right).